

UNIVERSITÀ DEGLI STUDI DI VERONA

DEPARTMENT OF NEUROLOGICAL AND MOVEMENT SCIENCES

GRADUATE SCHOOL OF SCIENCES ENGINEERING MEDICINE



DOCTORAL PROGRAM IN

MULTIMODAL IMAGING IN BIOMEDICINE

Cycle XXVI (2011 year)

PhD Thesis

MULTIMODAL TECHNIQUES FOR BIOMEDICAL IMAGE PROCESSING

S.S.D.ING-INF/06

Coordinator:

Prof. Andrea Sbarbati

Tutor:

Prof. Alberto Fenzi

PhD Student:

Dr. Fabio Amarù

Acknowledgements

At the end of this work I would like to thank all who have collaborated on the design and experimentation. There are many people who have contributed to this experience, in different ways. It is difficult to find the best words to express my gratitude and to thank everyone who has been in the right place at the right moment, but I'll try.

First of all I would like to thank my tutor Professor Alberto Fenzi who has led me during these years. I really appreciate that you have an open mind, which enhances communication and comparison of ideas both in scientific terms and daily life. I would like to express my gratitude for being present every time in my training. Moreover, I thank you for giving me the opportunity to make also an experience in an international laboratory, which are mentioned below.

I express my gratitude to my supervisor Professor Andrea Sbarbati as a good example of how to do research and for the helpful and constructive discussions we had in these years. I thank you for having encouraged me in the beginning of my research work and for awakening my curiosity about multimodal imaging in Biomedicine.

Life in Switzerland

I would like to thank the people I met in Switzerland, in the last period of my PhD.

Thanks to them, coming from different parts of the world, to have helped me to speak in English in academic class and in French Language outside, to have shared with them cultural, geographic, social aspects of life of the world.

Another thanks goes to Cristina Granziera for the availability and competence shown in the development of the paper at Ecole Polytechnique Federale de Lausanne, even more for the opportunity to enrich my competences participating to seminars, discussions, meetings in Siemens Group at Centre d'Imagerie Biomedicale at Lausanne.

A special thanks to my family. Words cannot express how grateful I am to my father and my sister for all of the sacrifices that you've made on my behalf. Your prayer for me was what sustained me thus far. At the end I would like to express appreciation to my beloved Silvia because

she always gave me strength to go on, she followed me and gave me encourage to continue the journey. In particular, I express to them my huge thanks to love given me to overcome and to fight an unexpected healthy problem, to have supported me psychologically

I would like to thank all my friends and colleagues, for the support they gave me. I am lucky because every time I moved and I started to live in a different place they made me feel at home. Together with them I have been and I still am discovering new cultures, learning new languages and growing into a more optimistic and patient person.

Fabio Amarù

Verona, 15 March 2014

*To my family,
for their constant support
and unconditional love*

Abstract

The PhD work involved three main biomedical research areas.

In the first, we aimed at assessing whether T1 relaxometry measurements may help identifying structural predictors of mild cognitive impairments in patients with relapsing-remitting multiple sclerosis. Twenty-nine healthy controls and forty-nine RRMS patients underwent at high resolution 3T magnetic resonance imaging to obtain optimal cortical and white matter lesion count/volume as well as T1 relaxation times (rt). In WML and CL type I (mixed white-gray matter), T1 rt z-scores were significantly longer than in HC tissue ($p < 0.001$ and $p < 0.01$ respectively), indicating loss of structure. Multivariate analysis revealed T1 rt z-scores in CL type I were independent predictors of long term retrieval ($p = 0.01$), T1 z-score relaxation time in white matter cortical lesions were independent predictors of sustained attention and information processing ($p = 0.02$);

In the second, we describe a biomagnetic susceptometer at room-temperature to quantify liver iron overload. By electronically modulated magnetic field, the magnetic system measure magnetic signal 10^8 times weaker than field applied. The mechanical noise of room-temperature susceptometer is cancelled and thermal drift is monitored by an automatic balance control system. We have tested and calibrated the system using cylindrical phantom filled with hexahydrated iron II chloride solution, obtaining the correlation ($R = 0.98$) of the maximum variation in the responses of the susceptometer. These measures indicate that the acquisition time must be less than 8 seconds to guarantee an output signal variability to about 4-5%, equal to $500 \mu\text{gr}/\text{gr}_{\text{wet}}$ of iron.

In the third, a 3D anatomically detailed finite element analysis human foot model is final results of density segmentation 3D reconstruction techniques applied in Computed Tomography(CT) scan DICOM standard images in conjunctions with 3D finite element analysis(FEA) modeling. In this model the real morphology of plantar fat pad has been considered: it was shown to play a very important role during the contact with the ground. To obtain the experimental data to compare the predictions of 3D foot model, a posturography static examination test on a baropodometric platform has been carried. The experimental plantar contact pressure is, qualita-

tively, comparable with FEA predicted results, nominally, the peak pressure value zones at the centre heel region and beneath the metatarsal heads.

Keywords:

High field MRI; T1 relaxation time; Multiple sclerosis; Cognitive impairment.

Room-temperature susceptometry; liver iron; thalassemia

Finite element Analysis; 3D Foot Model; CAD Modeling; plantar pressure

Riassunto

Il lavoro di dottorato ha coinvolto tre principali aree di ricerca biomedica.

Nella prima area, abbiamo mirato a valutare se le misure del tempo di rilassamento T1 in Risonanza Magnetica possono contribuire ad individuare dei predittori strutturali di lievi disturbi cognitivi in pazienti con forma Recidivante-Remittente di Sclerosi Multipla (RRMS). Ventinove controlli sani (HC) e quarantanove RRMS pazienti sono stati sottoposti a Risonanza magnetica a 3T per acquisire in maniera ottimale per la zona corticale e per la sostanza bianca (WML), i tempi di rilassamento T1 (rt), la conta delle lesioni e il volume. Nella WML e in quelle di tipo CL I (sostanza bianca - grigia mista), i T1 rt z-score sono risultati, significativamente, più lunghi rispetto ai tessuti dei controlli HC ($p < 0.001$ e $p < 0.01$, rispettivamente), indice di un'impoverimento del tessuto cerebrale. L'analisi di regressione multivariata ha rivelato che: i T1 rt z-score nelle lesioni corticali sono predittori indipendenti del recupero della memoria a lungo termine ($p = 0.01$), i T1 z-score nella lesioni corticali della materia bianca sono predittori indipendenti del deficit relativi all'attenzione prolungata e all'elaborazione delle informazioni ($p = 0,02$);

Nella seconda, descriviamo un suscettometro biomagnetico a temperatura ambiente in grado di quantificare il sovraccarico di ferro nel fegato. Tramite un campo magnetico modulato elettronicamente, il sistema riesce a misurare segnali magnetici 10^8 volte più piccoli del campo applicato. Il rumore meccanico del suscettometro a temperatura ambiente viene minimizzato e il drift termico viene monitorato da un sistema automatico di bilanciamento. Abbiamo testato e calibrato lo strumento utilizzando un fantoccio riempito con una soluzione di esacloruro esaidrato II di ferro, ottenendo come correlazione $R = 0,98$ tra la massima risposta del suscettometro e la concentrazione di ferro. Queste misure indicano che per garantire un buon funzionamento dello strumento con una variabilità del segnale di uscita pari al 4-5%, eguale a circa 500ugr/gr di ferro, il tempo di acquisizione deve essere minore o uguale a 8 secondi.

Nella terza area, un'analisi agli elementi finiti del modello 3D anatomicamente dettagliato del piede umano è il risultato finale della segmentazione 3D, secondo tecniche di ricostruzione applicate ad immagini standard DICOM di scansione a Tomografia Computerizzata, in congiunzione con la modellazione 3D assistita e dell'analisi agli elementi finiti (FEA). In questo modello la reale morfologia del cuscinetto adiposo plantare è stata considerata: è stato dimostrato

giocare un ruolo molto importante durante il contatto con il terreno. Per ottenere i dati sperimentali da confrontare con le predizioni del modello 3D del piede, un esame posturografico statico su una pedana baropodometrica è stato effettuato. La pressione sperimentale del contatto plantare è risultata, qualitativamente, comparabile con i risultati predetti dall'analisi agli elementi finiti, principalmente, confrontando i valori sperimentali con i valori massimi delle pressioni in corrispondenza delle zone centrali del tallone e sotto le teste metatarsali.

Parole chiave :

Risonanza Magnetica a 3T; Tempo di rilassamento T1; Sclerosi Multipla; Deficits cognitivi.

Suscettometria a Temperatura ambiente; ferro nel fegato; talassemia

Analisi agli elementi finiti; Modello 3D del piede; Modellazione CAD; pressione plantare

Contents

Acknowledgements	3
Abstract	6
Keywords:	7
Riassunto	8
Parole chiave :	9
Contents	10
List of Figures	13
List of Tables	15
Chapter 1 Introduction	16
1.1 Outline of Thesis	16
Chapter 2 Magnetic Resonance Imaging predictors of mild cognitive deficits in early relapsing-remitting multiple sclerosis	19
2.1 Abstract.....	19
2.2 Introduction	20
2.3 Methods	21
2.3.1 Subject population.....	21
2.3.2 Neuropsychological assessment	21
2.3.3 MRI data acquisition	22
2.3.4 Post-processing.....	22
2.3.5 Statistics	23
2.4 Results	24
2.4.1 Clinical and neuropsychological results.....	24
2.4.2 Cortical and subcortical lesions counts and T1 relaxation times.....	24
2.4.3 Neural correlates of neuropsychological deficits	24
2.5 Discussions	25
2.6 References	27
2.7 Tables.....	31

2.8	Figure.....	34
Chapter 3	A room-temperature susceptometer to measure liver iron concentration: data analysis, calibration and test	37
3.1	Abstract.....	37
3.2	Introduction	38
3.3	Metods	39
	3.3.1 Background and motivation	39
	3.3.2 The measurement system	40
	3.3.3 The electronic modulation.....	40
	3.3.4 The balancing coils.....	40
	3.3.5 The automatic balancing	41
	3.3.6 Susceptometer Layout	41
	3.3.7 Experimental testing setup	42
	3.3.8 Other aspects of liver suscptomtry	42
3.4	Results	43
	3.4.1 Electronic modulation : benefits and drawback	43
	3.4.2 Balancing results	43
	3.4.3 Stability of background signal: tests.....	44
	3.4.4 Calibration of Biosusceptometer	44
	3.4.5 Test of Waterbag	45
3.5	Discussions	45
3.6	Conclusions	46
3.7	References	47
3.8	Tables.....	49
3.9	Figure.....	51
Chapter 4	A Finite Element Analysis of 3D Anatomic Human Foot with plantar Fat Pad 60	
4.1	Abstract.....	60
4.2	Introduction	61
4.3	Metods	62
	4.3.1 Geometry Modelling	62
	4.3.2 Finite element Modeling	63
	4.3.3 Interactions between parts	64
	4.3.4 Property of Materials.....	65

4.3.5	Load and Boundary conditions.....	65
4.3.6	Mesh Generation	66
4.4	Results	66
4.5	Discussions	66
4.6	Conclusions	67
4.7	References	68
4.8	Tables.....	70
4.9	Figure.....	71

List of Figures

Figure 1: Double-Inversion Recovery (DIR) sequence	34
Figure 2: Two inversion-contrast magnetization-prepared rapid gradient echo (MP2RAGE) sequence	34
Figure 3: T1 from Two inversion-contrast magnetization-prepared rapid gradient echo (T1 map) sequence	34
Figure 4: 3-Dimensional Fluid Attenuated Inversion Recovery (3D FLAIR) sequence.....	35
Figure 5: Coregistration of MRI data into MP2RAGE space	35
Figure 6: T1Map and Lesions Union Mask	35
Figure 7: T1Map and Label Mask overlapped.....	36
Figure 8: T1Map and Spatial Atlas mask (as anatomical region) overlapped	36
Figure 9: Sensor unit.....	49
Figure 10: Electrostatic shield	49
Figure 11: Active balance coil L2C and passive balance coils L3 and L5 and resistor R3 ed R5 (config. I)	51
Figure 12: By changing the phase and the amplitude of the current in the coil L3A(config. II)	51
Figure 13: Active balance coils L2C and passive balance coils L4 with parallel resistor(config. III).....	52
Figure 14: Passive balance coils L3A and L3B(config. IV).....	52
Figure 15: Active balance coil L2C and passive balance coil L3C(config. V).....	53
Figure 16: Active balance coil L3A and passive balance coil L3B(config. VI).....	53
Figure 17: Active balance coil L1C and passive balance coil L4C(config. VII)	54
Figure 18: Flowchart of automatic balancing system	54
Figure 19: Susceptometer layout	55
Figure 20: FFT signal changing during 30 minutes (T_{room} from 24.5°C to 24.6°C).....	55
Figure 21: FFT signal changing during 30 minutes (T_{room} from 24.7°C to 24.8°C).....	56
Figure 22: FFT signal changing during 30 minutes (T_{room} from 24.1°C to 24.5°C).....	56

Figure 23: Acquisition timing (AIR – PHANTOM – AIR).....	57
Figure 24: Output acquisition signal (in up the output signal vs time, in down the FFT output signal vs time).....	57
Figure 25: Phantom filled with Ferric Chloride.....	58
Figure 26: Phantom filled with water	58
Figure 27: Calibration line: signal FFT(average value) versus concentrations	59
Figure 28: Latex Waterbag	59
Figure 29: Backward helix.....	71
Figure 30: Finite element Model of the Foot.....	71
Figure 31: A) Morphology of HFP B) sagittal section of HFP in spatial relationship with the heel and the Achilles tendon, C) axial section of HFP in connection with the plantar muscles, D) non-structured portion of HFP; E) front and rear sections.....	72
Figure 32: Loads and Boundary conditions	72
Figure 33: Workflow methodology for 3D Cad Modelling.....	73
Figure 34: 3D model of the foot with together all the bones and plantar FatPad	74
Figure 35: Left: Facet Joints of the calcaneus (and talus that articulates with the cuboid), right: the talus (by Drake, Vogl, Mitchell, Tibbitts and Rivhardson 2008).....	74
Figure 36: Interaction between the posterior inferior portion of the heel bone and fat pad (tie constrain interactions)	75
Figure 37: Interaction between the fat pad and the horizontal support.....	75
Figure 39: Global Mesh of 3D foot Model	76
Figure 38: Smooting step.....	76
Figure 40: FEA Predicted plantar pressure on the plantar fat pad.....	77
Figure 41: Experimental foot plantar contact pressure distribution on the baropodometric platform	77
Figure 42: Co-registration of FEA predicted contact pressure on the ground (in violet) into experimental contact pressure on the baropodometric platform (in green).....	78
Figure 43: Von Mises stress(pure compression).....	79
Figure 44: Foot section-cut (pure compression)	80
Figure 45: Von Mises Stress (pure compression) of plantar fat pad.....	81

List of Tables

Table 1: Neuropsychological testing.....	31
Table 2: Sequences Parameters.....	32
Table 3: Cognitive results of RRMS patients and controls.....	32
Table 4: Lesion Number, Lesion Volume, and T1 zscore relaxation time in Patients with Relapsing-Remitting Multiple Sclerosis	33
Table 5: Correlation coefficients (multivariate analysis) between MRI parameters and cognitive variables in patients with relapsing remitting multiple sclerosis	33
Table 6: Gradiometer parameters	49
Table 7: Measurement Protocol.....	49
Table 8: Concentrations simulate liver iron disease	50
Table 9: Properties of Materials.....	70
Table 10: Weight-bearing capacity of the fibula as a percentage of the total load. SG = strain gauge, FT force trasductors [7].....	70

Chapter 1 Introduction

1.1 Outline of Thesis

Analysis of multi-modality data is inherent to many problems in science and engineering including biomedical image analysis. Technologies for imaging are individually expensive, thus ways to synergistically derive information from complementary modalities have the potential to substantially enhance our understanding of underlying biological and medical processes. The field of multimodal biomedical imaging developed rapidly during the last decade and the surge of activity within the last decade is a simple proof of the exciting insights offered through the analysis of multimodal biomedical imaging data. Due to the increasing complexity, volume and modeling challenge of increasingly available multimodal biomedical imaging data, there is critical need for new, advanced multimedia signal processing, modeling and computational methods for fast, accurate and cost-effective analysis of multimodal biomedical data, to obtain comprehensive information about the underlying biomedical event and for faster acceptance of novel imaging modalities in real-world applications.

The goal of this work has been to show how in different field of medical imaging, multimodal techniques help to measure, quantify, correct, correlate, predict, discover aspects of human disease.

The Phd Doctoral Program has involved three main research areas: one of these was done in collaboration with a Consortium (FO.CA.VER) of companies active in the footwear Industry. Main achievements: companies received funds to go from footwear prototype to production. My work, also, included working with EPFL laboratory and with Siemens Healthcare Switzerland for a research project in multiple sclerosis disease.

The PhD Projects have been the followings:

1. “*MRI correlates of mild cognitive deficits in early relapsing-remitting multiple sclerosis*” – Signal Processing Laboratory(LTS5), EPFL, Lausanne, Switzerland:

Main acquired skills has been:

- Solid knowledge in Brain Imaging Analysis software

- Expertise in rigid and non-rigid registration of images (with FSL and/or Elastix)
 - Solid capability to analyze MRI-brain imaging data: lesions and volume count, T1 mapping evaluation, non-parametric statistical correlations (with MATLAB R2013b Unix and/or SPSS 22 Unix).
2. “*Non-invasive Determination of liver iron concentrations (LIC) with a Biosusceptometer at room temperature(RT)*” – Radiation and Protection Service, Verona, Italy

Main acquired skills has been:

- Development of a new methodology of automatic balancing of a gradiometer (magnetic sensor) at room- temperature (by using Pspice Circuit Simulation and NI-LabVIEW);
 - Structural Optimization of a mechanical modulated Biosusceptometer to measure liver iron concentration:
 - The activities involved choosing non-magnetic materials, building coil sensor, assembling the parts, acquiring software and testing.
3. “*Innovative shoes*” - Albo n. 221/2010 Prot. N.16066 del 24/03/2010 –Regione Veneto, Italy

Main acquired skills has been:

- Development of a new methodology of design of footwear based on the finite element;
- Foot DICOM Automatic Image Segmentation (by using AMIRA 5.3 semi-automatic blow tool)
- Foot 3D Cad Modeling (by using Rhinoceros, Rapidform, MeshLab, SolidWorks 2010)
- Development of a 3D mechanical foot model with ABAQUS 6.10 FEA;
- Validation of 3D model with baropodometric platform;

The topics of interest have included:

- Multimodal imaging techniques: data acquisition, reconstruction; 2D, 3D imaging, simultaneous imaging;
- Hardware/software design (*e.g.* Labview and CAD for bio-amplifier circuits)
- Preprocessing, denoising, filtering;
- Bio-image processing (*e.g.*, visualization, segmentation, registration)
- Multimodal signal processing and data fusion;

- Multivariate methods and array analysis;
- Statistical analysis (*e.g.*, parametric and non-parametric methods, regression models);
- Multi-subject analysis, group analysis

Chapter 2 Magnetic Resonance Imaging predictors of mild cognitive deficits in early relapsing-remitting multiple sclerosis

2.1 Abstract

Background: Despite mild cognitive impairment is a known early feature of multiple sclerosis patients, the biological substrate of cognitive deficits in multiple sclerosis is still elusive.

Objective: We aimed at assessing whether T1 relaxometry measurements may help identifying structural predictors of mild cognitive impairments in patients with relapsing-remitting multiple sclerosis (RRMS).

Design: Cohort study

Setting: Hospital-based multiple sclerosis clinic

Participants: Twenty-nine healthy controls and forty-nine patients with relapsing-remitting multiple sclerosis.

Main Outcome Measures: All subjects underwent at 3T Magnetic Resonance Imaging including the following sequences: two inversion-contrast magnetization-prepared rapid gradient echo, double-inversion recovery and 3-dimensional fluid attenuated inversion recovery. The protocol was designed to maximise lesion detection in white and gray matter. T1 z-score values in the lesions, lesions number and lesions volume were calculated for gray matter cortical lesions, white matter subcortical lesions and mixed cortical lesions. For each patient, cognitive performance was tested using Brief Repeatable Battery of Neuropsychological Tests.

Results: Relapsing-remitting multiple sclerosis patients and healthy controls showed differences in age ($p < 0.01$) and in education ($p < 0.02$), but not in gender. T1 z-score values in white matter subcortical lesions and in mixed cortical lesions were consistently longer in lesions compared to non-lesion tissue in patients and in healthy tissue in controls ($p < 0.01$). Multivariate analysis revealed that: T1 z-score relaxation time in mixed cortical lesions ($\beta = 0.26$; $p < 0.01$) was

an independent predictors of consistency component of long term retrieval memory; T1 z-score relaxation time in white matter cortical lesions ($\beta=-0.29$; $p<0.05$) was an independent predictors of sustained attention and information processing; gender ($\beta=0.41$; $p<0.01$) and education ($\beta=0.05$; $p<0.01$) were independent predictors of semantic verbal fluency ($r^2=0.25$; $p=0.01$).

Conclusions: T1 relaxation times provide with a sensitive measure of the microstructural brain alterations underlying mild cognitive impairment in early multiple sclerosis. The tissue loss in cortical, subcortical targets shows to be associated with cognitive dysfunctions in relapsing-remitting multiple sclerosis.

2.2 Introduction

Cognitive impairment affects approximately 40% to 70% of the multiple sclerosis (MS) patients [1, 2]. Frequently affected functions include attention, information processing, executive functioning, processing speed and long-term memory [3]. Among these, information processing speed appears to be the most sensitive measure of cognitive deficits in early MS [4].

Magnetic resonance imaging (MRI) has been extensively exploited to investigate cognitive dysfunction in MS. Nonetheless, the underlying physiopathological mechanisms remain unclear [3, 5, 6].

Measures of whole-brain atrophy showed only moderate correlations with cognitive dysfunction [3, 6]. Likewise, the correlations between the extents of white matter (WM) abnormalities detected on conventional brain MRI and cognitive impairment are generally low [7-10].

In this context, cortical pathology has recently received more attention. Thanks to the recently developed Double Inversion Recovery (DIR) MRI sequence, it is now possible to detect cortical lesions (CLs) in vivo [11-14], and the number of CLs correlates better with MS-related cognitive impairment than the number of WM lesions [15-17]. Moreover, cortical atrophy has been reported to have a higher impact than whole-brain atrophy on both physical disability [18, 19] and cognitive impairment [20]. Altogether, however, grey matter pathology appears to only partially explain cognitive deficits in MS patients.

Despite the fact that most of the published studies focused on patients with well-established RRMS (> 6 years disease duration) or on SPMS patients with moderate to severe cognitive dysfunction, current measures of pathological changes in MS (lesion number, volume, atrophy) do not seem to provide with adequate information.

In this context, other non-invasive MRI markers of disease impact and progression may be more sensitive and may hence be helpful to clarify the structural correlates of cognitive dysfunction in MS. Quantitative measurements of T1 relaxation times provide with markers of subtle micro-

structural damage as well as with microstructural characteristics of lesion tissue. T1 relaxation times allow distinguishing lesions from normal-appearing white matter in patients and non-pathological brain tissue in controls [21-23]. As to lesions characterisation, longer T1 values have been previously reported to indicate loss of tissue structure, whereas T1-shortening may correspond to pathological processes like accumulation of methemoglobin, proteinaceous material, lipids, free radicals, paramagnetic metals (non-heme iron) and remyelination [23].

To date, no studies have attempted at correlating early cognitive deficits in MS patients with T1 characteristics of lesion tissue of both cortical and subcortical lesions.

This work investigates a cohort of early RRMS patients with subtle cognitive symptoms. The aim is to test the hypothesis that T1 relaxation times of particular brain regions (namely cortical and subcortical lesions) provide with a sensitive and useful tool to study the substrates of cognitive deficits in MS.

2.3 Methods

2.3.1 Subject population

Forty-nine patients (14 males and 35 females) with early RRMS according to the McDonald criteria [24, 25] (age: 34.2 ± 8.8 y; mean educational level: 15.2 ± 2.9 y; disease duration: 2.9 ± 1.9 y; EDSS disability score: 1.6 ± 0.3) participated in the study. Patients with a diagnosis of major depression or other psychiatric disorders according to the DSM-IV criteria were not considered.

The control group consisted of twenty-nine healthy volunteers (8 males and 21 females - mean age: 32.3 ± 8.3 y; mean educational level: 16.7 ± 3.2 y) with no history of alcohol or drug abuse, major psychiatric disorders (major depression, psychosis, untreated bipolar disorders), head trauma, other neurological disorders or systemic illness.

All participants underwent a neuropsychological examination and brain MRI. The study was approved by the local Ethics Committee and all subjects gave informed consent for their participation.

2.3.2 Neuropsychological assessment

All participants underwent the Brief Repeatable Battery of Neuropsychological Tests (BRB-N) [26]. In brief, the BRB-N is composed of the following tests. The Selective Reminding

Test (SRT) measures verbal learning and delayed recall through presentation of a list of 12 words and five subsequent learning trials: the SRT distinguished between short-term and long-term components of memory and examines also the consistency of retrieval from long-term memory. We used in this study three indices: the SRT-long term storage in which a word is recalled on consecutive trials, the consistent long term retrieval (CLTR) in which a word is consistently recalled on all subsequent trials and the Delayed recall (SRTD) is the total number of words recalled after an 11 minute delay. The 10/36 spatial recall test (SPART) assesses visual learning and recall by recreating the pattern of 10 checkers on a 6´6 checkerboard viewed for 10 seconds. The symbol digit modalities test (SDMT) measures complex attention and concentration by requiring the subject to associate symbols with numbers and quickly generate the number when shown the symbol during 90 seconds. The paced auditory serial addition task (PASAT) evaluates sustained attention and information processing speed, and is measured by asking the patient to add each number to the one immediately preceding it while numbers are presented every three seconds. The word list generation (WLG) measures semantic verbal fluency, evaluating the spontaneous production of words beginning with a particular letter during 60 seconds. The complete set of neuropsychological tests is presented in Table 1.

Mood symptoms and fatigue were quantified using the Hospital Anxiety and Depression scale [27] [28] and the Fatigue Scale for Motor and Cognitive functions (FSMC) [29], respectively.

2.3.3 MRI data acquisition

Within two weeks from neuropsychological assessment, participants underwent brain MRI at 3T (Magnetom Trio a Tim System, Siemens Healthcare, Germany) using a commercial 32-channel head coil. The acquisition protocol was conceived in order to maximise lesion detection in WM and GM as well as in the cerebrum and the cerebellum.

The imaging protocol included the double-inversion recovery (DIR, T2-weighted, suppressing signals from both WM and CSF, [11], Figure 1), the two inversion-contrast magnetization-prepared rapid gradient echo (MP2RAGE - 3D T1-weighted providing T1 maps from the same scan, [30], Figure 2) and the 3-dimensional fluid attenuated inversion recovery (3D FLAIR T2-weighted, see[31], Figure 4). For sequence details see Table 2.

2.3.4 Post-processing

A certified neurologist and a certified neuroradiologist identified [32] the lesions by consensus in all contrasts separately. Subsequently, the lesions were manually contoured and assigned to one of the following classes: cerebral GM (cortical lesion type II, CL II), cerebral WM, mixed cerebral GM/WM(cortical lesion type I, CL I). The identified lesions were manual-

ly delineated by a trained technician. The resulting mask were finally double-checked and, if necessary, corrected by the study physicians (Figure 7, Figure 8).

The imaging volume and lesion masks were patient-wise co registered (Figure 5) to a common image space using a home-built-rigid-body registration software. Subsequently, a single set union mask was created per patient containing all lesions from all contrasts with their maximal spatial extent. MRI parameters that were evaluated are lesion number, volume and T1 relaxation times: these one last were evaluated for each contrast and for a mask representing the set union (Figure 6) of all the contrast lesion masks. The segmented masks were applied to the T1-maps from the MP2RAGE (Figure 3).

Finally, for each patient only T1 mean relaxation times of cortical, subcortical and mixed lesions were standardized as follows:

$$\frac{\mu_i - \mu_{HC}}{\sigma_i} \quad (1)$$

where: μ_i is the T1 mean relaxation times of each region, σ_i is the standard deviation of T1 relaxation time of whole region of interest in healthy controls and μ_{HC} is the T1 mean relaxation time of whole region of interest in healthy controls.

2.3.5 Statistics

Kruskal-Wallis test was used to compare demographic, clinical, behavioural findings between patients and controls. A Box-Cox transformation was applied to all cognitive variable and MRI parameters (lesion number and volume) in order to normalise the data prior to analysis.

A general linear model regression was applied to evaluate the association between all cognitive scores as outcome variables and population (age and education) and MRI scores (T1 z-score relaxation time, lesion number and volume) as predictors. Backward stepwise analyses were conducted with the Wald criterion using with $p=0.05$ for entry level and $p=0.10$ for removal. Bonferroni correction was applied for multiple comparison. The significant variables were identified with $p\text{-value} < 0.05$. All statistical analysis was performed using MATLAB R2013a Statistical Toolbox.

2.4 Results

2.4.1 Clinical and neuropsychological results

No between-group difference found for gender($p=0.87$) and age($p=0.12$). However, RRMS patients and controls differed in education (i.e. years of study, $p=0.02$)

The cognitive impairment results of all patients are reported in Table 3. Patients showed on average significantly low scores on measure of information processing speed (p -value =0.005 after correction for multiple comparisons)

Concerning the behavioural questionnaires, RRMS patients and controls had comparable scores on the HAD scale (depression: $p=0.006$); on the other hand, patients showed higher scores of fatigue on the total FSMC score ($z=7.82$, $p=1*10e-12$ after correction for multiple comparisons) both on the physical dimension of the scale ($p=0.0013$) and on its cognitive dimension ($p=6*10^{-5}$).

2.4.2 Cortical and subcortical lesions counts and T1 relaxation times

All early RRMS patients showed cortical lesions (CLs), whereas no CLs were observed in healthy controls. The majority consisted of CLs and mixed cortical-subcortical lesions, see Table 4. The rest of the CLs were characterised as type II (intra-cortical lesions). No type III/IV lesions (large subpial lesions) were detected. Furthermore, almost all patients showed a substantial number of subcortical lesions.

T1 z-score relaxation times of cortical and subcortical lesions in the cerebral hemispheres and the cerebellum are reported in Table 4. Except for the pure cortical (CL-II and cerebellum) lesions, T1 z-score values were consistently longer in lesions compared to non-lesion tissue in patients and in healthy tissue in controls ($p<0.01$).

2.4.3 Neural correlates of neuropsychological deficits

T1 relaxation times of MS lesions

The correlations coefficients between MRI parameters and cognitive measurement are reported in Table 5. Stepwise regression analysis applied on all patients revealed significant independent contributions from gender ($\beta=-0.27$; $p<0.05$), T1 z-score relaxation time in mixed cortical lesions ($\beta=0.26$; $p<0.01$) and gray matter cortical lesions number ($\beta=-0.29$; $p<0.05$) as a predictors (final model with $r^2=0.28$; $F=5.25$; $p=0.02$ after correction for multiple comparisons) of consistency component of long term retrieval memory. Education ($\beta=0.49$; $p<0.01$) and T1 z-score relaxation time in white matter cortical lesions($\beta=-0.29$; $p<0.05$) were found to be independent predictors of sustained attention and information processing ($r^2=0.24$; $F=7.18$; $p=0.02$ after correction for multiple comparisons). In the end, gender ($\beta=0.41$; $p<0.01$) and education

($\beta=0.05$; $p<0.01$) were independent predictors of semantic verbal fluency ($r^2=0.25$; $F=7.81$; $p=0.01$).

No correlations were found between SRT-D, SRT-LTS, SPART and SPART-D and MRI parameters of gray, white and mixed matter lesions.

2.5 Discussions

In this study, we show that the microstructural characteristics of cortical and subcortical lesions, as measured by T1 relaxation times, correlate positively with consistency of long-term memory in patients with early RRMS. In addition, we also give evidence that T1 relaxation times of cortical hemispheric and cerebellar lesions negative correlate with attention and information processing dysfunction in the same patients.

The measured T1 values of WM and GM in healthy controls are in agreement with recent publication [33-35]: pure cortical lesion(CL-II) T1 results did not reach significance between lesion tissue in patients, healthy controls and normal-appearing tissue; instead, statistical differences were found between lesion tissue, non-lesion tissue in patients and in healthy tissue in controls in cerebral and cerebellar WM as well as CL-I and mixed cerebellar GM/WM lesions

T1 MRI measurements are globally influenced by pathological changes of different severity, such as demyelination, gliosis, inflammation, axonal injury and axonal loss [27, 33-35]. In acute MS lesions, there is first a prolongation of T1 and T2 due to acute oedema, rapidly followed by shortening of both relaxation times [36]. On the other hand, relaxation times are quite variable in chronic plaques, indicating pathological heterogeneity [36]. Traditionally, T1 relaxation time measurements have been exploited in MS to assess the degree of tissue alteration in different MS subtypes [21, 22, 27, 37]. Moreover, they provide a quantitative measure that correlates moderately with global disability scores in MS (i.e. EDSS) [21, 38] and MS Functional composite (MSFC) score [39]. So far, however, there are no studies attempting at achieving better clinic-radiological correlations by combining T1 relaxation times of both cortical and subcortical lesions.

This study explores the hypothesis that T1 relaxation times are sensitive correlates of cognitive dysfunction, also in early phases of MS. We studied a cohort of RRMS patients with disease duration inferior to 6 years, who benefitted of a complete clinical and neurological examination. Comparing the patient group to the control group, we detected mild cognitive deficits in sustained attention and information processing speed (impaired performance in PASAT), as well as in consistency of long-term memory (impaired performance in SRT-CLTR) in the investigated

patient cohort. These results are in line with previous studies reporting that attention deficits occur frequently in MS from the early stages of the disease [1, 3, 5, 10, 40-42].

Visual attention and information processing are functions controlled by a widespread network involving frontal and parietal association cortices, the connections between them and the cerebellum [43]. By contrast, executive control is known to crucially involve the prefrontal cortex, the cerebellum and the fronto-cerebellar connectivity complex [44, 45].

Our data show a correlation between the normalised T1 values of hemispheric lesions (cortical and subcortical) and the SRT-CLTR test, assessing long term retrieval memory. On the other hand, the mean T1 relaxation times of hemispheric and cerebellar cortical lesions correlated with the PASAT test that assesses sustained attention and processing speed. These results indicate that, in our cohort of MS patients, the degree of damage in the cortex and in the white matter is related to the presence of memory deficits. In addition, our findings suggest that the characteristics of the cortical lesions in the hemispheres and the cerebellum influence the presence of attention deficits.

The observed correlations were negative and showed that lower attention deficits are concomitant with longer T1-relaxation times. These findings point at the fact that a certain threshold of tissue loss, as measured by prolonged T1, is necessary to activate compensatory mechanisms in early RRMS. In MS, compensatory adaptive mechanisms were previously observed in several domains using functional MRI, i.e. in the motor system [46] and in the working memory system [10]. The attention network has also been previously shown to functionally remodel through the recruitment of areas normally involved in high-level cognitive processing in order to guarantee normal or sub-normal attention performances in RRMS patients [40, 47]. In our cohort of patients, it is plausible that tissue loss in targeted cortical, subcortical or cerebellar regions induced functional changes in the attention and the memory networks in order to allow the recruitment of supplementary areas and to preserve normal cognitive performance.

In summary, we showed that T1 relaxation studies in early MS stages may provide with sensitive radiological markers to elucidate the substrate of already mild deficits.

2.6 References

1. Rao, S.M., et al., *Cognitive dysfunction in multiple sclerosis. I. Frequency, patterns, and prediction*. Neurology, 1991. **41**(5): p. 685-91.
2. Peyser, J.M., et al., *Guidelines for neuropsychological research in multiple sclerosis*. Archives of neurology, 1990. **47**(1): p. 94-7.
3. Chiaravalloti, N.D. and J. DeLuca, *Cognitive impairment in multiple sclerosis*. Lancet Neurol, 2008. **7**(12): p. 1139-51.
4. Amato, M.P., V. Zipoli, and E. Portaccio, *Cognitive changes in multiple sclerosis*. Expert review of neurotherapeutics, 2008. **8**(10): p. 1585-96.
5. Amato, M.P., V. Zipoli, and E. Portaccio, *Multiple sclerosis-related cognitive changes: a review of cross-sectional and longitudinal studies*. J Neurol Sci, 2006. **245**(1-2): p. 41-6.
6. Rovaris, M., G. Comi, and M. Filippi, *MRI markers of destructive pathology in multiple sclerosis-related cognitive dysfunction*. Journal of the neurological sciences, 2006. **245**(1-2): p. 111-6.
7. Berg, D., et al., *Lesion pattern in patients with multiple sclerosis and depression*. Multiple sclerosis, 2000. **6**(3): p. 156-62.
8. Rao, S.M., et al., *Correlation of magnetic resonance imaging with neuropsychological testing in multiple sclerosis*. Neurology, 1989. **39**(2 Pt 1): p. 161-6.
9. Swirsky-Sacchetti, T., et al., *Neuropsychological and structural brain lesions in multiple sclerosis: a regional analysis*. Neurology, 1992. **42**(7): p. 1291-5.
10. Mainero, C., et al., *fMRI evidence of brain reorganization during attention and memory tasks in multiple sclerosis*. Neuroimage, 2004. **21**(3): p. 858-67.
11. Geurts, J.J., et al., *Intracortical lesions in multiple sclerosis: improved detection with 3D double inversion-recovery MR imaging*. Radiology, 2005. **236**(1): p. 254-60.
12. Pouwels, P.J., et al., *Human gray matter: feasibility of single-slab 3D double inversion-recovery high-spatial-resolution MR imaging*. Radiology, 2006. **241**(3): p. 873-9.
13. Filippi, M., et al., *Intracortical lesions: relevance for new MRI diagnostic criteria for multiple sclerosis*. Neurology, 2010. **75**(22): p. 1988-94.
14. Simon, B., et al., *Improved in vivo detection of cortical lesions in multiple sclerosis using double inversion recovery MR imaging at 3 Tesla*. Eur Radiol, 2010. **20**(7): p. 1675-83.
15. Calabrese, M., et al., *Cortical lesions and atrophy associated with cognitive impairment in relapsing-remitting multiple sclerosis*. Arch Neurol, 2009. **66**(9): p. 1144-50.
16. Calabrese, M., M. Filippi, and P. Gallo, *Cortical lesions in multiple sclerosis*. Nat Rev Neurol, 2010.

17. Roosendaal, S.D., et al., *Accumulation of cortical lesions in MS: relation with cognitive impairment*. *Mult Scler*, 2009. **15**(6): p. 708-14.
18. De Stefano, N., et al., *Evidence of early cortical atrophy in MS: relevance to white matter changes and disability*. *Neurology*, 2003. **60**(7): p. 1157-62.
19. Calabrese, M., et al., *Evidence for relative cortical sparing in benign multiple sclerosis: a longitudinal magnetic resonance imaging study*. *Mult Scler*, 2009. **15**(1): p. 36-41.
20. Amato, M.P., et al., *Neocortical volume decrease in relapsing-remitting MS patients with mild cognitive impairment*. *Neurology*, 2004. **63**(1): p. 89-93.
21. Parry, A., et al., *White matter and lesion T1 relaxation times increase in parallel and correlate with disability in multiple sclerosis*. *J Neurol*, 2002. **249**(9): p. 1279-86.
22. Castriota-Scanderbeg, A., et al., *T1 relaxation maps allow differentiation between pathologic tissue subsets in relapsing-remitting and secondary progressive multiple sclerosis*. *Mult Scler*, 2004. **10**(5): p. 556-61.
23. Bakshi, R., et al., *Imaging of multiple sclerosis: role in neurotherapeutics*. *NeuroRx*, 2005. **2**(2): p. 277-303.
24. McDonald, W.I., et al., *Recommended diagnostic criteria for multiple sclerosis: guidelines from the International Panel on the diagnosis of multiple sclerosis*. *Ann Neurol*, 2001. **50**(1): p. 121-7.
25. Polman, C.H., et al., *Diagnostic criteria for multiple sclerosis: 2005 revisions to the "McDonald Criteria"*. *Ann Neurol*, 2005. **58**(6): p. 840-6.
26. Rao, S.M., *A manual for the Brief Repeatable Battery of Neuropsychological Tests in multiple sclerosis*. 1990, Medical College of Wisconsin: Milwaukee.
27. Davies, G.R., et al., *Normal-appearing grey and white matter T1 abnormality in early relapsing-remitting multiple sclerosis: a longitudinal study*. *Mult Scler*, 2007. **13**(2): p. 169-77.
28. Zigmond, A.S. and R.P. Snaith, *The hospital anxiety and depression scale*. *Acta Psychiatr Scand*, 1983. **67**(6): p. 361-70.
29. Penner, I.K., et al., *The Fatigue Scale for Motor and Cognitive Functions (FSMC): validation of a new instrument to assess multiple sclerosis-related fatigue*. *Mult Scler*, 2009. **15**(12): p. 1509-17.
30. Marques, J.P., et al., *MP2RAGE, a self bias-field corrected sequence for improved segmentation and T1-mapping at high field*. *Neuroimage*, 2010. **49**(2): p. 1271-81.
31. Mugler, J.P., 3rd, et al., *Optimized single-slab three-dimensional spin-echo MR imaging of the brain*. *Radiology*, 2000. **216**(3): p. 891-9.
32. Kober, T., et al., *MP2RAGE multiple sclerosis magnetic resonance imaging at 3 T*. *Invest Radiol*, 2012. **47**(6): p. 346-52.

33. van Waesberghe, J.H., et al., *Axonal loss in multiple sclerosis lesions: magnetic resonance imaging insights into substrates of disability*. *Ann Neurol*, 1999. **46**(5): p. 747-54.
34. Bitsch, A., et al., *A longitudinal MRI study of histopathologically defined hypointense multiple sclerosis lesions*. *Ann Neurol*, 2001. **49**(6): p. 793-6.
35. Laule, C., et al., *Water content and myelin water fraction in multiple sclerosis. A T2 relaxation study*. *J Neurol*, 2004. **251**(3): p. 284-93.
36. Larsson, H.B., et al., *Assessment of demyelination, edema, and gliosis by in vivo determination of T1 and T2 in the brain of patients with acute attack of multiple sclerosis*. *Magn Reson Med*, 1989. **11**(3): p. 337-48.
37. Manfredonia, F., et al., *Normal-appearing brain t1 relaxation time predicts disability in early primary progressive multiple sclerosis*. *Arch Neurol*, 2007. **64**(3): p. 411-5.
38. Papadopoulos, K., et al., *T1-relaxation time changes over five years in relapsing-remitting multiple sclerosis*. *Mult Scler*, 2010. **16**(4): p. 427-33.
39. Vrenken, H., et al., *Whole-brain T1 mapping in multiple sclerosis: global changes of normal-appearing gray and white matter*. *Radiology*, 2006. **240**(3): p. 811-20.
40. Staffen, W., et al., *Cognitive function and fMRI in patients with multiple sclerosis: evidence for compensatory cortical activation during an attention task*. *Brain : a journal of neurology*, 2002. **125**(Pt 6): p. 1275-82.
41. Rao, S.M., *Neuropsychology of multiple sclerosis*. *Current opinion in neurology*, 1995. **8**(3): p. 216-20.
42. Audoin, B., et al., *Compensatory cortical activation observed by fMRI during a cognitive task at the earliest stage of MS*. *Human brain mapping*, 2003. **20**(2): p. 51-8.
43. Allen, G., et al., *Attentional activation of the cerebellum independent of motor involvement*. *Science*, 1997. **275**(5308): p. 1940-3.
44. Schmahmann, J.D. and J.C. Sherman, *The cerebellar cognitive affective syndrome*. *Brain : a journal of neurology*, 1998. **121** (Pt 4): p. 561-79.
45. Baillieux, H., et al., *Cerebellar neurocognition: insights into the bottom of the brain*. *Clinical neurology and neurosurgery*, 2008. **110**(8): p. 763-73.
46. Rocca, M.A., et al., *Abnormal connectivity of the sensorimotor network in patients with MS: a multicenter fMRI study*. *Human brain mapping*, 2009. **30**(8): p. 2412-25.
47. Penner, I.K., et al., *Analysis of impairment related functional architecture in MS patients during performance of different attention tasks*. *Journal of neurology*, 2003. **250**(4): p. 461-72.

48. Staffen, W., et al., *Cognitive function and fMRI in patients with multiple sclerosis: evidence for compensatory cortical activation during an attention task*. *Brain*, 2002. **125**(Pt 6): p. 1275-82.

2.7 Tables

BRB-N Tests	
Cognitive variables	Cognitive Functions
SRT-CLTR	Verbal learning and memory: Consistency of Retrieval from Long-Term memory component
SRT-D	Verbal learning and memory: Delayed recall component
SRT-LTS	Verbal learning and memory Long-Term Storage component
SDMT	Processing speed and working memory
PASAT	Sustained attention and information processing speed
SPART	Visuospatial learning and recall
SPART-D	Visuospatial learning and Delayed recall
WLG	Semantic verbal fluency test

BRB-N Tests= Brief Repeatable Battery of Neuropsychological Tests

Abbreviations: SRT-CLTR=Selective Reminding Test–Consistent Long-term Retrieval; SRT-D=Selective Reminding Test–Delayed Recall; SRT-LTS=Selective Reminding Test–Long-term Storage; SDMT= Symbol Digit Modalities Test; PASAT= Paced Auditory Serial Addition Test at 3 seconds; SPART=10/36 Spatial Recall Test; SPART-D=10/36 Spatial Recall Test–Delayed; WLG=Word List Generation;

Table 1: Neuropsychological testing

Sequences Parameters			
	3D FLAIR	MP2RAGE	DIR
Acquisition	3D	3D	3D
Resolution	1 x 1 x 1.2 mm ³	1 x 1 x 1.2 mm ³	1.1 x 1 x 1.2 mm ³
Orientation/readout	Sagittal/ A >> P		
Matrix size	240 x 256	240 x 256	240 x 256
Slice/partitions	176	176	160
Acquisition time	6 min 27 s	8 min 22 s	12 min 52 s
No patients/controls scans	49/29	49/29	49/29
Acceleration factor	2	3	2
TE, ms	394	2.89	218
Inversion time(s), ms	1800	700/2500	3650
Flip angle(s), degrees	VFL*	4	VFL*
Echo/readout train length, ms	835	1162	640
TR, ms	5000	5000	10000
Bandwidth, Hz/pixels	781	240	651

Table 2. Sequence Parameters(continued)

Abbreviations: 3DFLAIR=3-Dimensional Fluid Attenuated Inversion Recovery; MP2RAGE= two inversion-contrast magnetization-prepared rapid gradient echo; DIR=double-inversion recovery. Parameters of all employed imaging sequences. All 3D contrasts were acquired with the same spatial resolution. *Optimized variable flip angle(VFL) pattern over the readout train. TE indicates echo time; TR, repetition time.

Table 2: Sequences Parameters

Characteristics	RRMS patients (p=49)	Healthy controls (c=29)	Adjusted p-value
SRT-LTS	62.5 ± 6.82	64.5 ± 6.5	0.2
SRT-CLTR	56.6 ± 11.1	59.9 ± 9.7	0.2
SRT-D	11.2 ± 1.14	11.5 ± 0.9	0.1
SPART	23.4 ± 4.3	23.3 ± 4.6	7.2
SPART-D	8.6 ± 2.05	8.6 ± 1.8	7.2
SDMT	56.9 ± 9.56	59.6 ± 11.4	0.8
PASAT	46.8 ± 10.8	51.9 ± 10.5	0.005
WLG	27.7 ± 5.3	28.7 ± 6.9	2.4

Abbreviations: SRT-LTS=Selective Reminding Test-Long-term Storage; SRT-CLTR=Selective Reminding Test-Consistent Long-term Retrieval; SRT-D=Selective Reminding Test-Delayed Recall; SDMT= Symbol Digit Modalities Test; PASAT= Paced Auditory Serial Addition Test at 3 seconds; SPART=10/36 Spatial Recall Test; SPART-D=10/36 Spatial Recall Test-Delayed; WLG=Word List Generation; Adjusted p-value for multiple comparison are reported

Table 3: Cognitive results of RRMS patients and controls.

MRI Lesions Classification	Lesions Number		Lesions Volume		T1 zscore relaxation time	
	mean	sd	mean	sd	mean	sd
WM lesions	36.89	27.81	3424.40	2892.72	10.27	4.66
GM cortical lesions	1.07	1.72	36.22	65.56	1.93	5.64
CLs type I	4.96	6.49	368.53	508.96	2.64	7.33

Abbreviations: WM= white-matter; GM= gray-matter; CLs=cortical lesions; sd=standard deviation;

Table 4: Lesion Number, Lesion Volume, and T1 zscore relaxation time in Patients with Relapsing-Remitting Multiple Sclerosis

Cognitive variable of BRB-N Tests	Multiple linear regression (β)											R square	F statistics	Model p-value
	Gender	Education	WM lesions T1 z-score	WM lesions mean Number	WM lesions mean Volume	GM lesions T1 z-score	GM lesions mean Number	GM lesions mean Volume	GM-WM lesions T1 z-score	GM-WM lesions mean Number	GM-WM lesions mean Volume			
SRT-CLTR	-0.27*	NS	NS	NS	NS	NS	-0.29*	NS	0.26*	NS	NS	0.28	5.25	0.02
SRT-D	NS	NS	NS	NS	NS	NS	NS	NS	NS	NS	NS	-	-	-
SRT-LTS	NS	NS	NS	NS	NS	NS	NS	NS	NS	NS	NS	-	-	-
SDMT	NS	NS	NS	NS	NS	NS	NS	NS	NS	NS	NS	-	-	-
PASAT	NS	0.49**	-0.29*	NS	NS	NS	NS	NS	NS	NS	NS	0.24	7.18	0.02
SPART	NS	NS	NS	NS	NS	NS	NS	NS	NS	NS	NS	-	-	-
SPART-D	NS	NS	NS	NS	NS	NS	NS	NS	NS	NS	NS	-	-	-
WLG	0.41*	0.05**	NS	NS	NS	NS	NS	NS	NS	NS	NS	0.25	7.81	0.01

Abbreviations: BRB-N Tests= Brief Repeatable Battery of Neuropsychological Tests; WM=white matter cortical lesions; GM=gray matter cortical lesions; GM-WM=gray-white(mixed) cortical lesions

SRT-CLTR=Selective Reminding Test–Consistent Long-term Retrieval; SRT-D=Selective Reminding Test–Delayed Recall; SRT-LTS=Selective Reminding Test–Long-term Storage; SDMT= Symbol Digit Modalities Test ;PASAT= Paced Auditory Serial Addition Test at 3 seconds; SPART=10/36 Spatial Recall Test; SPART-D=10/36 Spatial Recall Test–Delayed; WLG=Word List Generation.

NS=not significant,* $p < 0.05$,** $p < 0.01$; Model p-value is corrected for multiple comparison

Table 5: Correlation coefficients (multivariate analysis) between MRI parameters and cognitive variables in patients with relapsing remitting multiple sclerosis

2.8 Figure

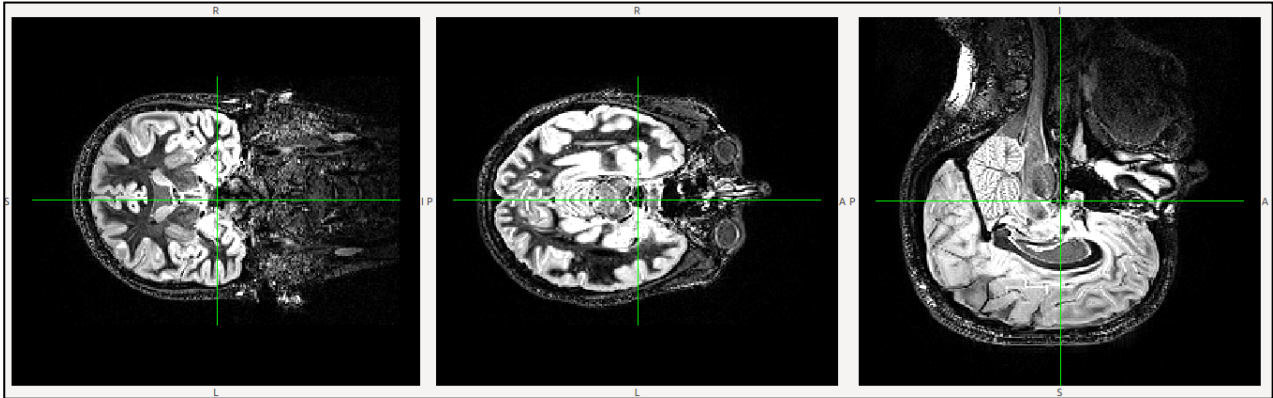


Figure 1: Double-Inversion Recovery (DIR) sequence

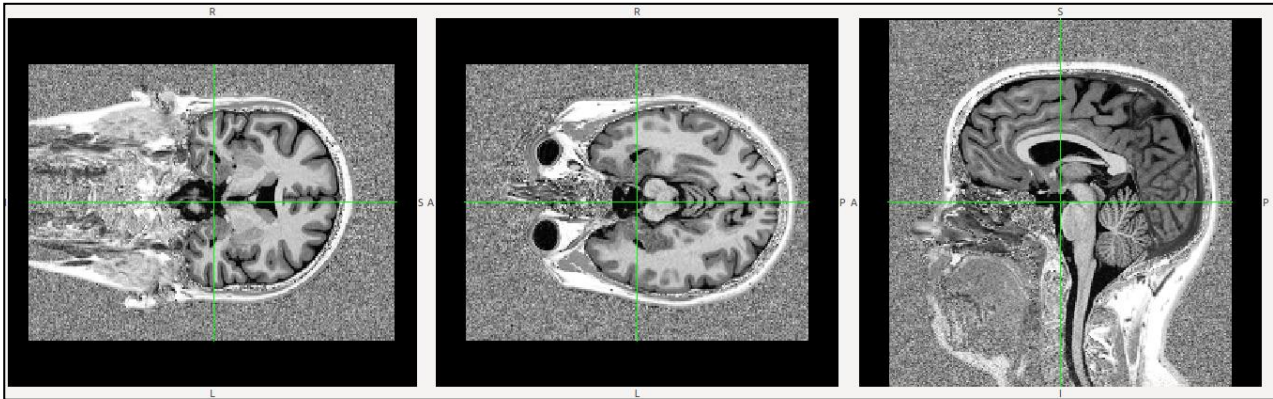


Figure 2: Two inversion-contrast magnetization-prepared rapid gradient echo (MP2RAGE) sequence

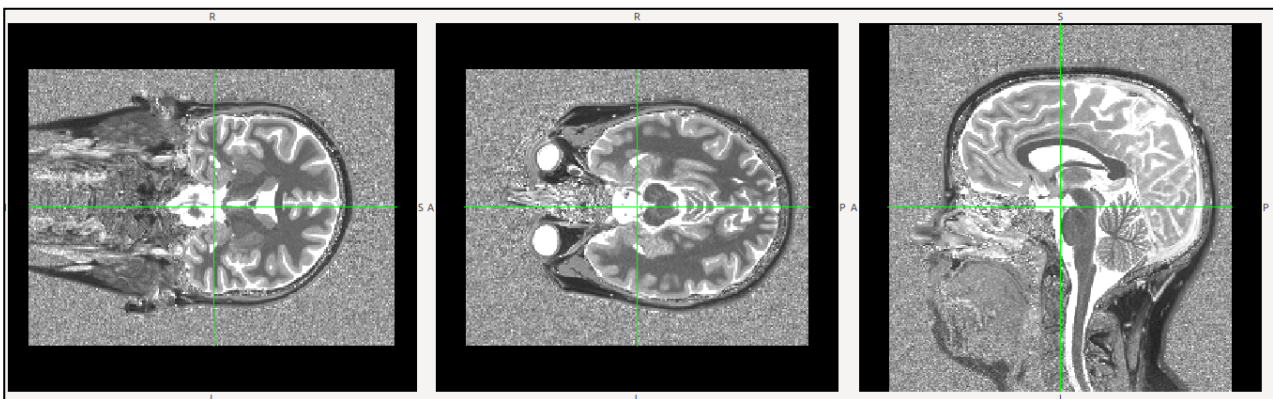


Figure 3: T1 from Two inversion-contrast magnetization-prepared rapid gradient echo (T1 map) sequence

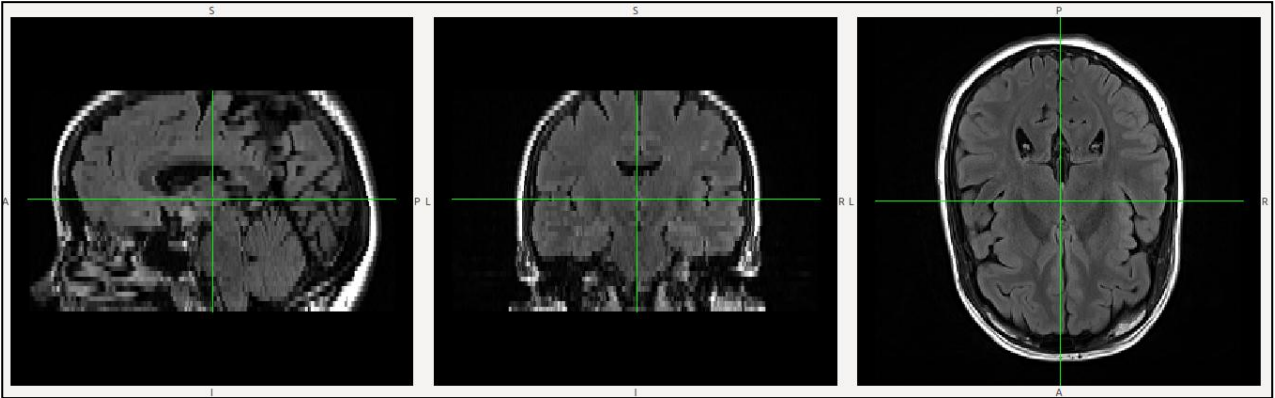


Figure 4: 3-Dimensional Fluid Attenuated Inversion Recovery (3D FLAIR) sequence

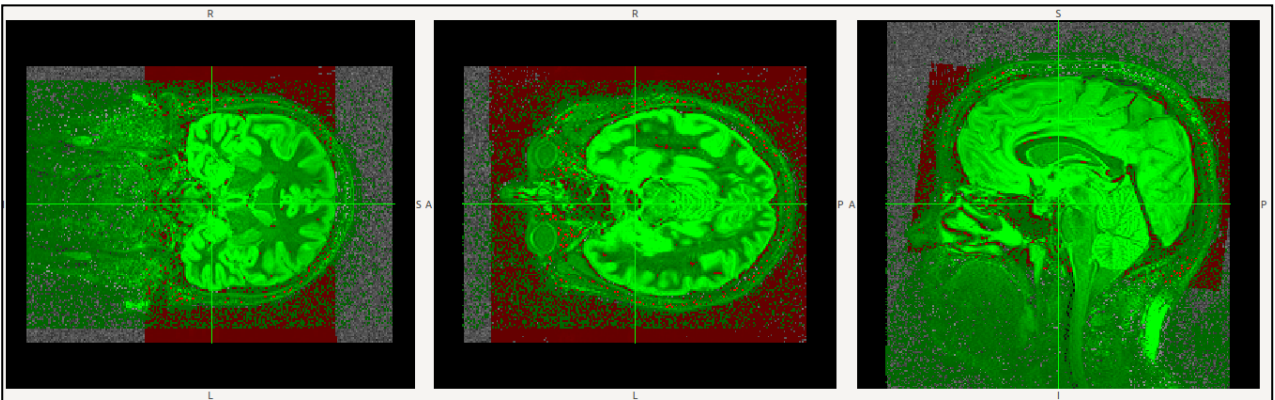


Figure 5: Coregistration of MRI data into MP2RAGE space

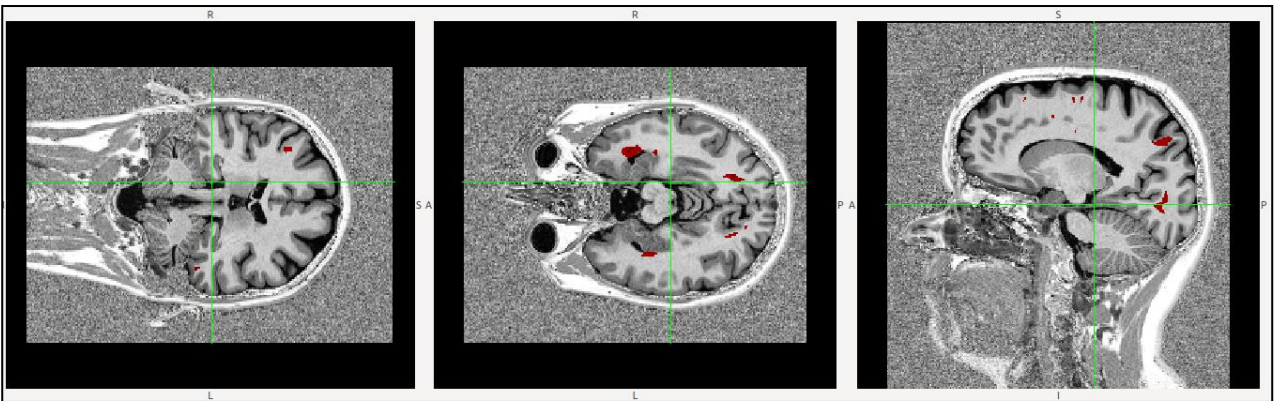


Figure 6: T1Map and Lesions Union Mask

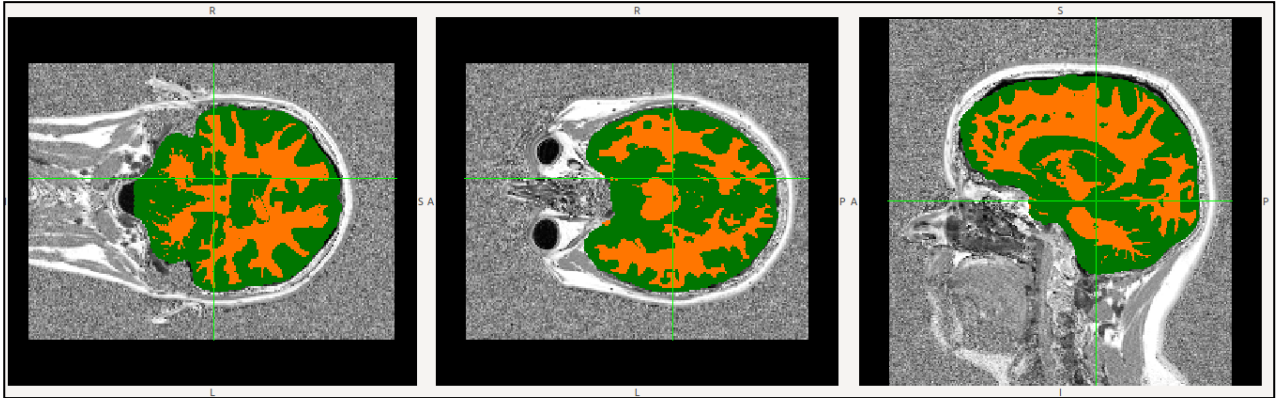


Figure 7: T1Map and Label Mask overlapped

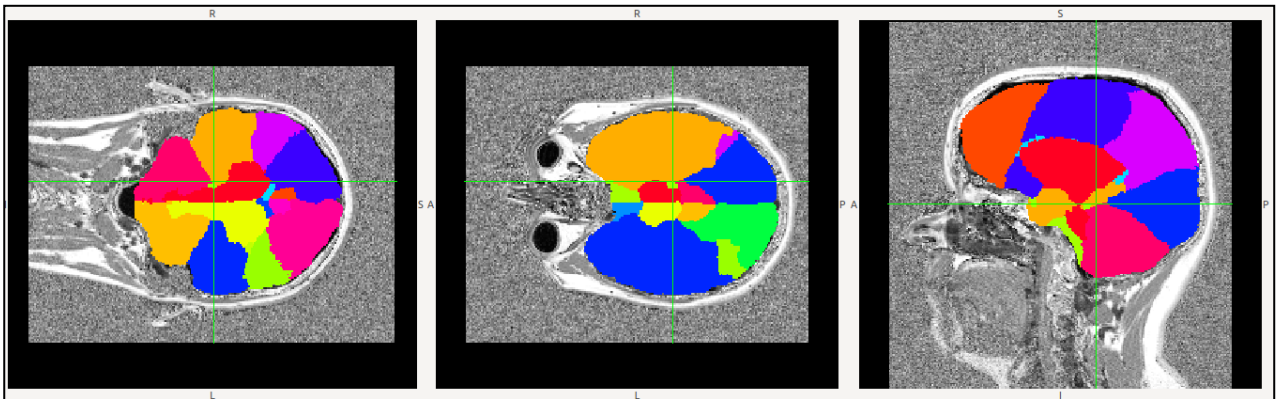


Figure 8: T1Map and Spatial Atlas mask (as anatomical region) overlapped

Chapter 3 A room-temperature susceptometer to measure liver iron concentration: data analysis, calibration and test

3.1 Abstract

Background: The determination of iron overload in the human body is essential for the management of therapies in different diseases characterized by iron accumulation. Until to now, the current room temperature mechanical-modulated susceptometer provides to do this but produces unexpected noisy signal.

Objective: We aimed at assessing whether a room-temperature electronic-modulated susceptometer may help measuring and monitoring the accumulation of iron.

Design: An AC susceptometer operating in the range of 1Hz to 600Hz at room temperature is designed, built and tested to measure concentration of ferric chloride in order to simulate the accumulation of liver iron. To remove mechanical noise an electronic modulation has been used.

Setting: To ensure a solid working of system the balancing condition is required, both during background measurements and during liver measurements: we have used a feedback control digital circuit to maintain the system in balancing conditions. The calibration and the test was carried out using solutions of ferric chloride in order to simulate different iron overloads.

Results: We have tested and calibrated the system using cylindrical phantom filled with hexahydrated iron II chloride solution, obtaining the correlation ($R=0.98$) of the maximum variation in the responses of the susceptometer. We have obtained that the acquisition time of measurement must be less than 8 seconds to guarantee a variability of the signal to about 4-5%.

Conclusions: Our room-temperature susceptometer uses oscillatory magnetic fields and cancels the signal from the applied field. It cancels, also, mechanical noise by electronic modulation of field, periodically, to simulate the motion toward the samples. Ferric chloride measurements indicate instrumental noise comparable with errors of the room temperature (RT) susceptometer.

3.2 Introduction

The determination of iron overload in the human body is essential for the management of therapies in different diseases characterized by iron accumulation. Its effects are especially clear in hereditary hemochromatosis and in transfusion-dependent patients with thalassemia major, where severely elevated iron can cause heart failure, diabetes, cirrhosis or liver cancer, and survival may depend on removing iron by phlebotomy or chelation(1).

Patients, who suffer from these diseases, don't succeed in producing blood cells and therefore require periodic transfusions; the iron received from transfused blood and not reused, because of disease, to produce new red blood cells, accumulates mainly in the liver. Liver biopsy is the traditional method for determining liver iron, is painful and carries a risk of severe bleeding (2, 3).

To avoid these risks, liver iron concentration can be measured non-invasively by magnetic resonance imaging (MRI) and biomagnetic liver susceptometry. However, these methods also have their own limitations of cost, accessibility and accuracy.

One advantage of MRI is that thousands of MRI scanners already exist. However, MRI scans still cost hundreds of dollars, and may involve delays in scheduling the scan and waiting for results. In addition, MRI senses iron indirectly, through its effect on the magnetic resonance of nearby water molecules (4). This interaction is complicated, poorly understood and dependent on a variety of factors such as tissue hydration, proton mobility and the clustering of iron deposits (4,5). However, recent studies have found good correlations with liver biopsy (6, 7).

Today's clinical susceptometers use SQUID magnetic sensors and superconducting field coils enclosed in a liquid-helium dewar (10). This classic design has been validated by liver biopsy (11), used clinically on hundreds of patients, and subjected to an intensive analysis of measurement errors (12).

Our measurement system used for monitoring and measuring the accumulation of iron in the liver is the Room Temperature(RT) mechanical-modulated Biosusceptometer(8). One of the problems that limits the performance of this machine is the instability of the signal caused by motion of the magnetic sensor. The motion is used in order to cancel the thermal drifts of the coils and to maintain the system in balance conditions. The use of this technique generates unexpected mechanical noise.

Currently there aren't in the bibliography alternative methods to solve the problem: in consequence of this, we have used the electronic modulation different to the mechanical modulation in order to remove mechanical noise and used a feedback control circuit to maintain the system in

balancing condition. Essential condition for ensuring a good working of the system is to maintain the balancing condition both during the time of background measurement (bi-distilled water) and during the time liver measurement: at this purpose we have tested several different protocols and after accurate laboratory measurements we have obtained that the time of measurement must be short in order to guarantee a stability of the signal. In this paper we have tested the stability of this system with the electronic modulation and with the automatic balancing. The test was carried out using the chloride II iron concentrations in order to simulate liver iron overloads.

3.3 Metods

3.3.1 Background and motivation

Compared to Magnetic Resonance, the susceptometry applied to the liver is difficult, because the magnetic field produced from the iron in the liver is 10^7 or 10^8 times smaller than the field we apply to the patient. This small response must be measured in the presence of the applied field. During measurement, the signal of the liver can easily be obscured by the field produced by small changes in temperature, from possible changes in the geometry of the coils that generate the field, the gain of the sensor, the geometric relationship between the sensor and the applied field.

SQUID susceptometers address these problems by exploiting the low noise of SQUID magnetic sensors, the stable magnetic fields produced by persistent currents in superconducting coils, and the stable geometry of source and sensing coils immersed in liquid helium(9).

These problems need to be overcome and resolved when we use a susceptometer at room temperature. In particular, the thermal variations of the surrounding environment produce a residue field, which is very small compared to that applied to the patient but comparable with that measured by the measuring coils (sensing). This signal slowly varying amplitude, most likely due to drifts in temperature that cause geometric deformations between the source and the sensing coils. To avoid such fluctuations in the signal to be measured, the current instrument was implemented a modulation technique mechanics, in particular the transmitting and the receiving coil is moved at 1Hz frequency above and below the patient. By using the concept of modulation they(8) managed to separate the signal component due to the thermal drift from that of the useful signal. The periodic oscillation of the coil allows with good approximation to minimize the noise components due to thermal drifts and to the effects of thermal expansion, but it produces in the output signal of sense coils noise components at the frequency of 21-22-23 Hz (RelazioneTecnica AR-FSE: Codice prog. 1695/1/11/1268/2008).

3.3.2 The measurement system

Our measurement system consists by two parts: the first one (source coils) generates the magnetic field, the second one (sense coils) detects the magnetic field produced by the liver and cancels the field produced by source. The magnetic sensor used is a gradiometer, in which the transmitter coil is a magnetometer, the receiver coil is a second order gradiometer. The coil system parameters to generate the field and to receive are described in Table 6: they are a compromise that permits to maximize the response to the magnetization of the liver and that minimizes the effects of abdominal tissue overlayer, decreasing the sensitivity of the probe in the pick up coils, the signal produced by lung, placed in proximity of the liver. The sensor has shown in Figure 9: the geometric dimensions are 16 and 2.5 centimeters, height and radius, respectively.

To ensure the magnetic sensor measures the liver magnetic susceptibility and not the electrical capacitance of the body, it is useful to shield the coils from electric fields: these electric fields can be capacitively coupled with the receiving coils and produce a shift in the measurement of the magnetic field. At this purpose, the magnetic sensor has shielded by electric fields, with an electrostatic shield (Figure 10).

3.3.3 The electronic modulation

Our modulation technique consists to keep the sensor in stationary position and to create the variation of the magnetic field through the generation of modulated electronically signals. The electronic modulation frequency is equal to that of the frequency of mechanical modulation(8). Our signal is the product of two signals: the carrier, a signal mathematically predetermined at 1 Hz frequency, and a modulating signal at 610 Hz frequency. This method permits to simulate the reciprocating motion of coil unit used by ref(8) device. With oscillating magnetic fields, we aimed that cancellation of the applied-field signal and simulated motion of the coil unit, permit to minimize sensor noise, applied-field fluctuations, and effects of thermal expansion.

3.3.4 The balancing coils

When the imbalance of the output voltage is higher than the desired resolution for measurements of magnetic susceptibility on the liver, it needs to compensate appropriately. To minimize these errors, we evaluated and built a system for automatic compensation, to produce a magnetic field opposite in phase to that produced.

Such compensation system must, mainly, cancel the produced field by non-perfect symmetry in the construction of the sensing coils, and after, it must ensure automatically the maintenance of

the condition of balance when the temperature changes become significant (more than 10^{-6} volt to gradiometer output). Bibliographical studies suggest that in order to obtain an optimum cancellation of the residual field it needs to eliminate in-phase and out-phase component of input signal.

For this purpose, we have studied and evaluated different circuit configurations (Figure :

- I. Active balance coil L2C and passive balance coils L3 and L5 with parallel R3 and R5 resistors (Figure 11) ;

By changing the phase and the amplitude of the current in the coil L3A (

- II. Figure 12);
- III. Active balance coils L2C and passive balance coils L4 with parallel resistor (Figure 13);
- IV. Passive balance coils L3A and L3B (Figure 14);
- V. Active balance coil L2C and passive balance coil L3C (Figure 15);
- VI. Active balance coil L3A and passive balance coil L3B (Figure 16);
- VII. Active balance coil L1C and passive balance coil L4C (Figure 17);

Active balance coil is powered-supply, instead, passive balance coil is inducted-current.

3.3.5 The automatic balancing

The output signals of the magnetic sensor are processed via a National Instrument acquisition board (NI-6289). In particular, the output signal is sent to a lock-in amplifier and a digital filter that, every second, extract in-phase and in-quadrature component of output signal: FFT norm and the sign of the unbalance signal. The compensation is automatic both on in-phase signal component and on in-quadrature other one, alternately every second. The FFT value is compared with a threshold value ($1 \cdot 10^{-5}$), under which the compensation doesn't work and above which, the compensation increases or decreases by one step the digital resistor: the increasing or decreasing depends to the sign of the output voltage.

The implementation of automatic control is made with NI-LabView software with a flowchart (Figure 18).

3.3.6 Susceptometer Layout

Figure 19 is a picture of Room Temperature electronic-modulated susceptometer. The coils are enclosed in a rigid fiberglass cylinder, which is lowered down to touch the phantom (like patient's abdomen). A water bag (not shown) fills any gaps between this enclosure and the phantom. During magnetic susceptibility measurements, the coil is stationary and the electronic

modulation simulates that the unit moves up and down within the outer cylinder. The susceptometer also includes a waveform generator to produce a 610-Hz sinewave (Hewlett Packard 33102a), an amplifier to drive the source coils (AE Techron 5050), signal pre-amplifiers of our own design, data acquisition cards, and a personal computer to demodulate the 610-Hz signal and calculate the ferric concentration.

3.3.7 Experimental testing setup

The measurement system is a Biosusceptometer Laboratory at room temperature. In Figure 16 the structure of susceptometer is presented with balancing and signal conditioning circuits. The control signal is digital. The balancing circuit works for canceling the in-phase and in-quadrature component of the input signal(8). Samples used for measurements are the plexiglass phantoms(

Figure 25), filled properly with ferric chloride in order to simulate the accumulation of iron in the liver. The measure of the liver iron accumulation normally is deduced by the subtraction of liver signal FFT and the signal background(like bi-distilled water) FFT. The solution that simulates liver iron is the a hexahydrated iron II chloride solution $\text{FeCl}_3 \cdot 6 \text{H}_2\text{O}$ in different concentrations (Table 8). For each solution the protocol was repeated cyclically (about 20-time) (Table 7); The plexiglass phantom was filled with a different concentration of ferric chloride and cleaned each time. The acquisition step air-phantom-air can be easily described with the following sequence(Figure 23): before the phantom is outside, then the phantom is placed under coil for 10 seconds and after the phantom is again outside.

3.3.8 Other aspects of liver susceptometry

3.3.8.1 Water-bag methods

In liver susceptometry, the response of liver iron is superimposed on a background signal due to the diamagnetism of the patient's body. This diamagnetic background is as large as the signal from liver iron at a concentration of several thousand $\mu\text{g/gwet}$, and is different for each patient because it depends from shape of the body.

To compensate for the body's diamagnetic response, we use a water-bag technique similar to that used with existing SQUID susceptometers (13, 14). The water bag fills the space between the patient's body and the rigid shell that encloses the susceptometer coils.

This waterbag needs to be filled with water when it did the background measurement and it needs to be emptied partly when the patients is placed down : therefore, during these phases in order to not introduce errors in measurement, it needs to not create air bubbles inside.

Consequently we have studied a better solution that has the advantages of last one and ensures a rapid membrane deformation without applying high pressure on the patient. The solution is shown in

Figure 28, in which it's represented the structure that contains the magnetic sensor and in particular the nose that will contain the magnetic sensor, the cylindrical container and the latex membrane.

3.4 Results

3.4.1 Electronic modulation : benefits and drawback

The continuous room temperature changings (from 24°C to 26°C) cause inevitable deformations in the geometry of the receiver coil, and changings in the induced magnetic field. In fact, as described in ref (8): "Thermally induced dimensional changes represent a challenging problem when you do differential measurements with high resolution. For a given change in temperature, the change of the length of the conductor is proportional to the coefficient of thermal expansion of the material involved".

By eliminating the motion of coil we obtain as improvement the cancelling of mechanical noise, but it needs to keep the temperature as stable as possible.

Thermal drifts are a problem when the source coils are electrically modulated, rather than mechanically. Although the mechanical movement significantly reduces the thermal drifts of the coils, we found that the 1°C changing of room temperature during working mechanical modulation introduces 2% variability of background signal, 5% variability during electronic modulation working.

3.4.2 Balancing results

In Pspice Simulation we have tested several circuits configuration, described in 3.34 section, to balance gradiometer and we have obtained the results for the following configurations:

- I. This configuration allows to obtain a balance of the output voltage equal to 0.2nV;
- II. To obtain the balance, the phase of the current in balance coil must be equal to the phase of the current in source coil;
- III. To obtain balance condition ($V_{out} = 25.57\mu V$) it needs to have high value of potentiometer;
- IV. This method does not allow balance condition under 30mV;
- V. This method does not allow balance condition under 191 μV ;
- VI. This method allows balance condition equal to 0.61nV.

VII. This method allows balance condition equal to 0.2nV.

Definitively, the compensation methods implemented in real circuit are the following one:

1. L3A active balance coil and L3B passive balance coil;
2. L1C active balance coil and L4C passive balance coil;

The first method has the advantage as a minor influence on the unbalance of the detection coils, but the drawback that the passive coil is close to the sense coil (L5) that receives the signal from the liver, and therefore could affect the measurement on liver.

The second method has the advantage the long distance between the coil and the liver but the the drawback the greatest influence on the inbalance of the sense coils.

3.4.3 Stability of background signal: tests

The magnetic sensor has been physically performed and installed on an experimental probe. A very rigid structure was built in order to break down all the mechanical vibrations present on the structure (Figure 19)

In first instance, we tested the working of the automatic compensation by room temperature changing: initially we turned on the electronical-modulated signal, 30 minutes before taking measurements, as long as the coils get to thermal regime; after, we run automatic compensation and, so registered the air signal every 3 minutes for 30 minutes: the signal acquisition is acquired when the automatic balance is stopped. We registered 3 times the signal for each acquisition. From each acquisition we extracted the FFT mean value of output signal and the room temperature: we tested the changing of room temperature, under electronic modulation, before and after the automatic balance. During the first set the temperature changes from 24.5°C to 24.6°C (Figure 20), during the second one from 24.7°C to 24.8°C (Figure 21), during the third from 24,1°C to 24.5°C (Figure 22). During the first test the variability of the background[48] signal amounted to 1.23%, during the second amounted to 7.75%, during the third amounted to 3.60%.

Finally, the mean variation of the output signal FFT, when electronical-modulated signal and automatic compensation is turned on is 2.40%.

3.4.4 Calibration of Biosusceptometer

The tests show a linear relationship between FFT (Fast-Fourier Transformat) signals and concentration. The FFT value of each concentration expressed in the graph is the result of the subtraction between the backgroundwater) (Figure 26)signal FFT and the solution (Figure 25) (iron II Chloride) FFT signal. Figure 23 and Figure 24 show the variation in 1-Hz signal amplitude

over a period of 20 seconds. This is the result of filtered signal output from lock-in amplifier (demodulation signal in-phase).

The results were fitted via linear interpolation and we have obtained the following calibration line (Figure 27) for this electronic-modulated susceptometer. The measurement is differential and it's done by this expression:

$$\text{BACKGROUND}(\text{water}) - \text{PHANTOM}(\text{iron II chloride}) = \text{iron} [\text{ugr/gr}]$$

Calibration line is shown in Figure 4. The results are fitted linearly, we obtained a straight line with this expression :

con Coefficients (with 95% confidence bounds):

Goodness of fit:

The measures have a correlation coefficient equal to 0.98, meaning that this prototype is able with good precision to distinguish a ferric concentration from to .

3.4.5 Test of Waterbag

Tests carried out on the new waterbag showed good water tightness and the good deformability of latex membrane. This system also has the advantage to avoid air bubbles during the filling of the waterbag and permits faster measurements.

3.5 Discussions

A very important feature of this system is the ambient temperature changing during the several measurements (about $\pm 3^\circ\text{C}$ during all measurements, about $\pm 0.2^\circ\text{C}$ each three-four measurements): these small changes are a limit for this system at room temperature but the speed execution of measurement permits to maintain small the changes in temperature. Furthermore the acquisition air-phantom-air allows to monitor every 10 seconds the signal variability, and therefore, to avoid errors in measurement. This aspect constitutes a limit mainly in the measurement of the concentration of iron in the patient liver because the measurement must be carried out

quickly. A possible application of this system with patients is to built the system in a structure small and portable.

Water phantom measurements indicate instrumental noise about 4-5% which is small compared with other errors due to the response of the patient's body

For improvement the performance of the instrumentation and remove possible additional error, in addition to this system, is to be used a Locketor Loops: this magnetic sensor is able to evaluate the thickness of air between the patient abdomen and probe sensor.

Our room-temperature susceptometer uses oscillatory magnetic fields and reduces thermal drifts by automatic balancing and performs quickly the measurement.

Our hope is that this simplified susceptometer technology will make accurate, noninvasive body iron measurements more available.

3.6 Conclusions

Our room-temperature susceptometer uses oscillatory magnetic electronic-modulated fields and cancels the signal from the applied field. It reduces thermal drift and mechanical noise by using an electronic modulation of the signal applied to sample and by reducing the time acquisition. The correlation measurement shown a 0.98 R-square between the signal FFT and the concentration of ferric chloride. These results indicate that the fundamental error limits for the new system are similar to those of existing mechanical modulated susceptometer. Our hope is that simplified susceptometer technology will make accurate, with a flexible and portable instrument.

3.7 References

1. Brittenham GM, Badman DG. Noninvasive measurement of iron: report of an NIDDK workshop. *Blood*. 2003; 101:15–9. [PubMed: 12393526]
2. Cohen MB, A-Kader HH, Lambers D, Heubi JE. Complications of percutaneous liver biopsy in children. *Gastroenterology*. 1992; 102:629–32. [PubMed: 1732131]
3. Piccinino F, Sagnelli E, Pasquale G, Giusti G. Complications following percutaneous liver biopsy. A multicentre retrospective study on 68,276 biopsies. *J Hepatol*. 1986; 2:165–73. [PubMed: 3958472]
4. Jensen PD. Evaluation of iron overload. *Br J Haematol*. 2004; 124:697–711. [PubMed: 15009057]
5. Ghugre NR, Coates TD, Nelson MD, Wood JC. Mechanisms of tissue-iron relaxivity: Nuclear magnetic resonance studies of human liver biopsy specimens. *Magn Reson Med*. 2005; 54:1185–93. [PubMed: 16215963]
6. Wood JC, Enriquez C, Ghugre N, Tyzka JM, Carson S, Nelson MD, Coates TD. MRI R2 and R2* mapping accurately estimates hepatic iron concentration in transfusion-dependent thalassemia and sickle cell disease patients. *Blood*. 2005; 106:1460–5. [PubMed: 15860670]
7. St Pierre TG, Clark PR, Chua-anusorn W, Fleming AJ, Jeffrey GP, Olynyk JK, Potrakul P, Robins E, Lindeman R. Noninvasive measurement and imaging of liver iron concentrations using proton magnetic resonance. *Blood*. 2005; 105:855–61. [PubMed: 15256427]
8. A Room- Temperature Susceptometer to measure live iron: Susceptometer design and performance, S. Kumar, W F Avrin Quantum Magnetics, Inc., San Diego, CA, USA
9. Paulson DN, Fagaly RL, Toussaint RM, Fischer R. Biomagnetic susceptometer with SQUID instrumentation. *IEEE Trans Magn*. 1991; 27:3249–52.
10. Farrell DE, Tripp JH, Zanzucchi PE, Harris JW, Brittenham GM, Muir WA. Magnetic measurement of human iron stores. *IEEE Trans Magn*. 1980; 16:818–23.
11. Fischer, R.; Engelhardt, R.; Nielsen, P.; Gabbe, EE.; Heinrich, HC.; Schmiegel, WH.; Wurbs, D. Liver iron quantification in the diagnosis and therapy control of iron overload patients. In: Hoke, M., et al., editors. *Adv in Biomagnetism '91*. Amsterdam: Elsevier; 1992. p. 585-8.
12. Fischer, R.; Engelhardt, R.; Nielsen, P. In: Nowak, H., et al., editors. *The influence of thorax tissue in biomagnetic liver susceptometry*; *Biomag 2002: Proc. 13th Intl. Conf.*

- on Biomagnetism; Jena, Germany. 10–14 August 2002; Berlin: VDE Verlag GmbH; 2002. p. 1063-5.
13. Fischer R, Liver iron susceptometry, *Magnetism in Medicine : a Handbook* ad w Andae and H Nowak (Berlin, Wiley-VHC) pp.286-301
 14. Paulson D N, Fagaly R I et al. Biomagnetic susceptometer with SQUID instrumentation *IEEE Trans. Magn.* 27 3249-52

3.8 Tables



Coil	Coil Type	Turn coil	Coil name	Electrostatic shield
 <p>Figure 9: Sensor unit</p>	Sense Coil	+550	L3	 <p>Figure 10: Electrostatic shield</p>
	Active Feedback Balance Coil	+15	L3A	
	Source Coil	-100	L1	
	Feedback Coil	+15	L1A	
	Sensing Feedback Coil	+15	L1C	
	Sensing Feedback Coil	+15	L2C	
	Sense Coil	-1100	L4	
	Sensing Feedback Coil	+15	L3C	
	Sensing Feedback Coil	+15	L4C	
	Feedback Coil	+15	L1B	
	Source Coil	+100	L2	
	Passive Feedback Balance Coil	+15	L3B	
	Sense Coil	+550	L5	

Table 6: Gradiometer parameters

TYPE OF OPERATION	TIME DURATION
AUTOMATIC BALANCE: AIR MEASURE	120''
ACQUISITION: AIR – PHANTOM – AIR	20''

Table 7: Measurement Protocol

Solution Name	Concentration	Number of Measurement
SOL_D	490ugr/gr	60
SOL_B	981ugr/gr	60
SOL_A	2452ugr/gr	32
SOL_C	4904ugr/gr	60
H ₂ O	0ugr/gr	96

Table 8: Concentrations simulate liver iron disease

3.9 Figure

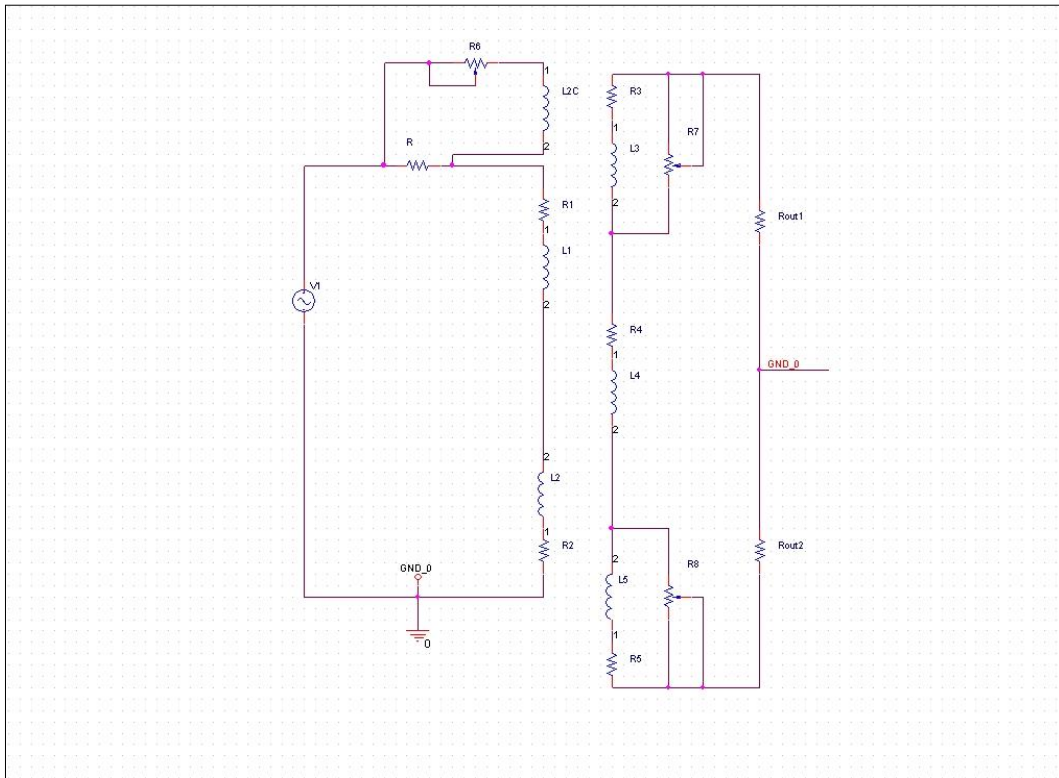


Figure 11: Active balance coil L2C and passive balance coils L3 and L5 and resistor R3 ed R5 (config. I)

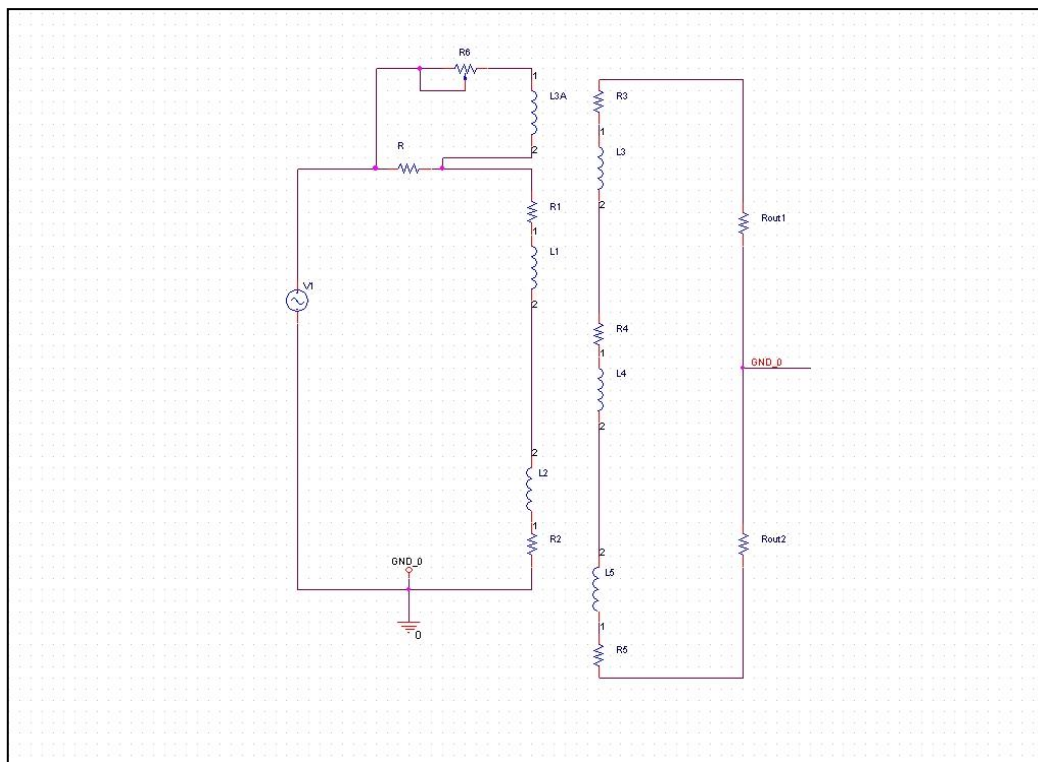


Figure 12: By changing the phase and the amplitude of the current in the coil L3A(config. II)

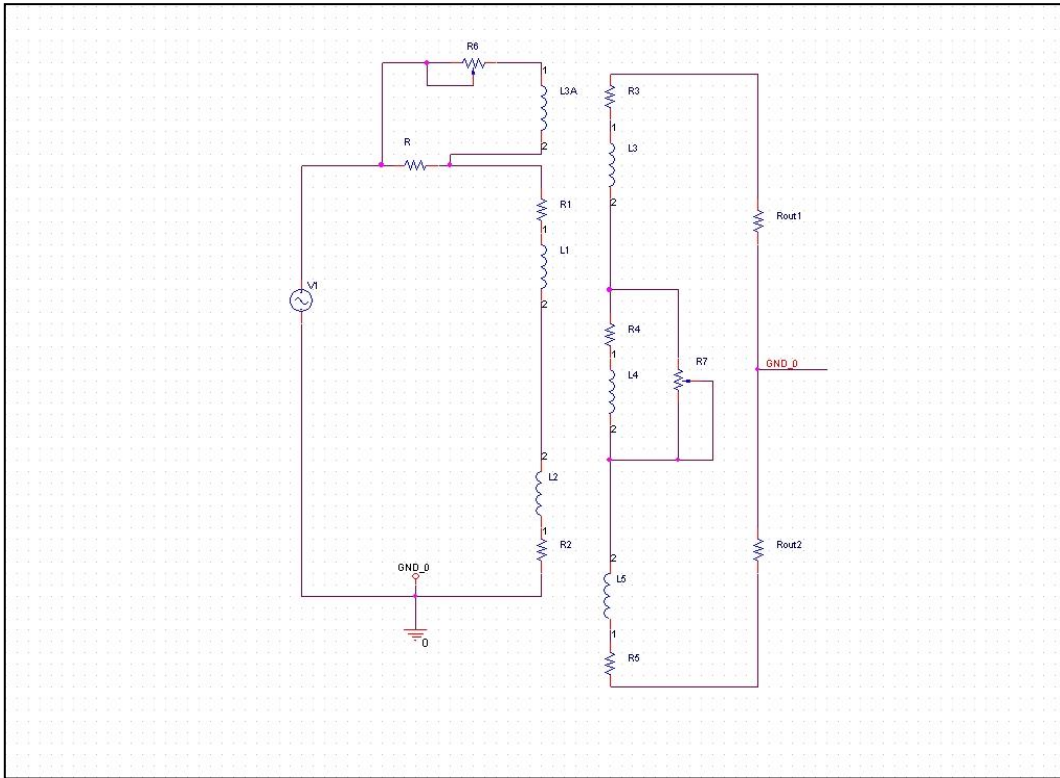


Figure 13: Active balance coils L2C and passive balance coils L4 with parallel resistor(config. III)

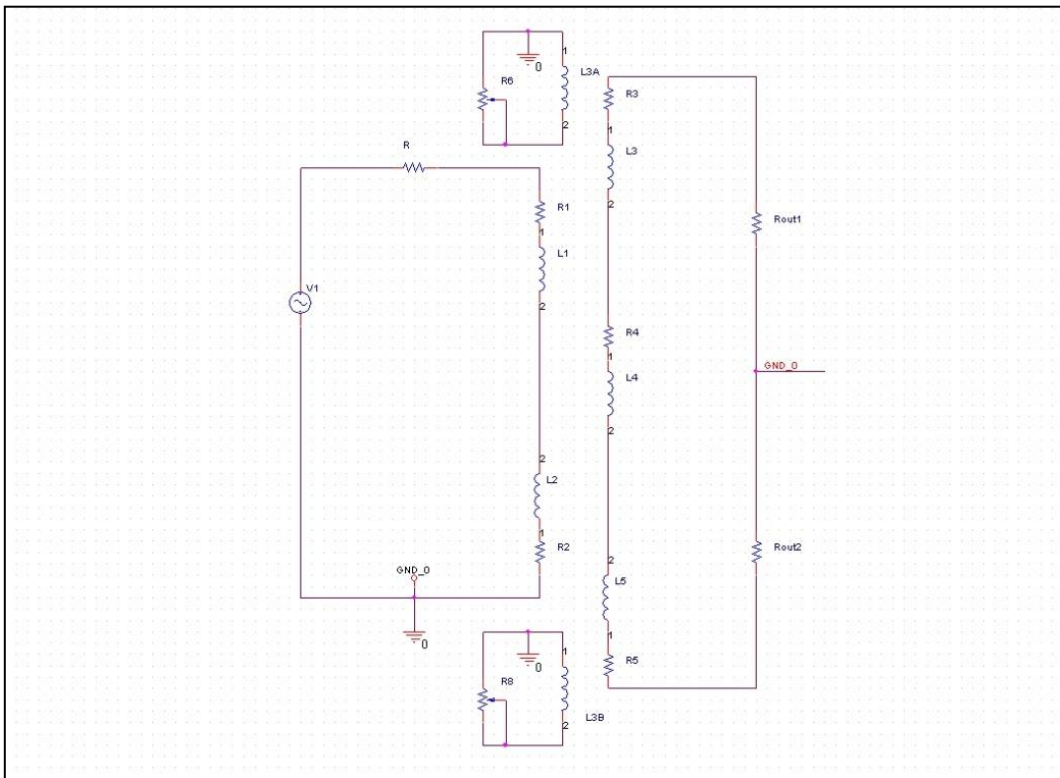


Figure 14: Passive balance coils L3A and L3B(config. IV)

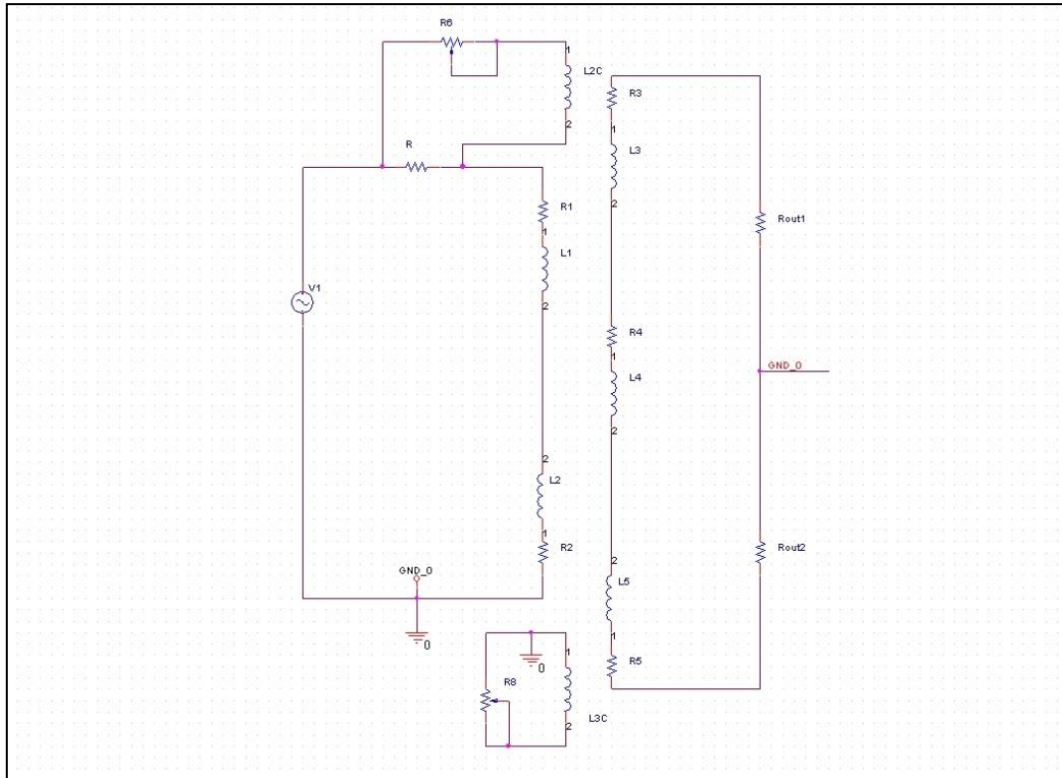


Figure 15: Active balance coil L2C and passive balance coil L3C(config. V)

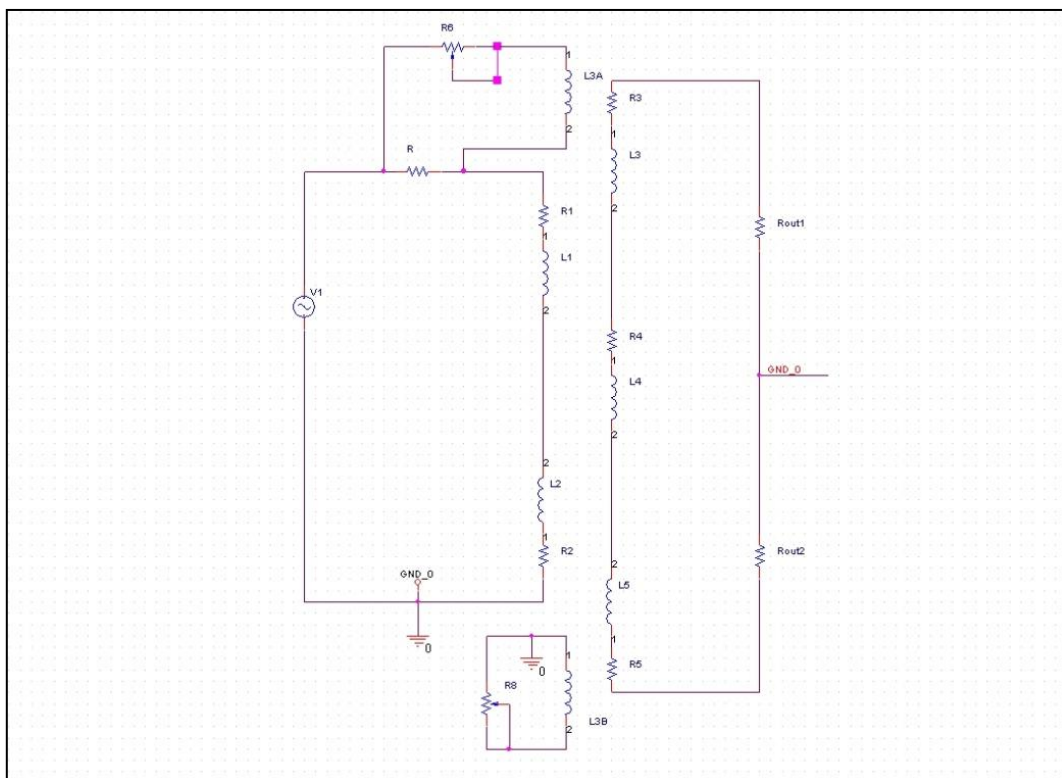


Figure 16: Active balance coil L3A and passive balance coil L3B(config. VI)

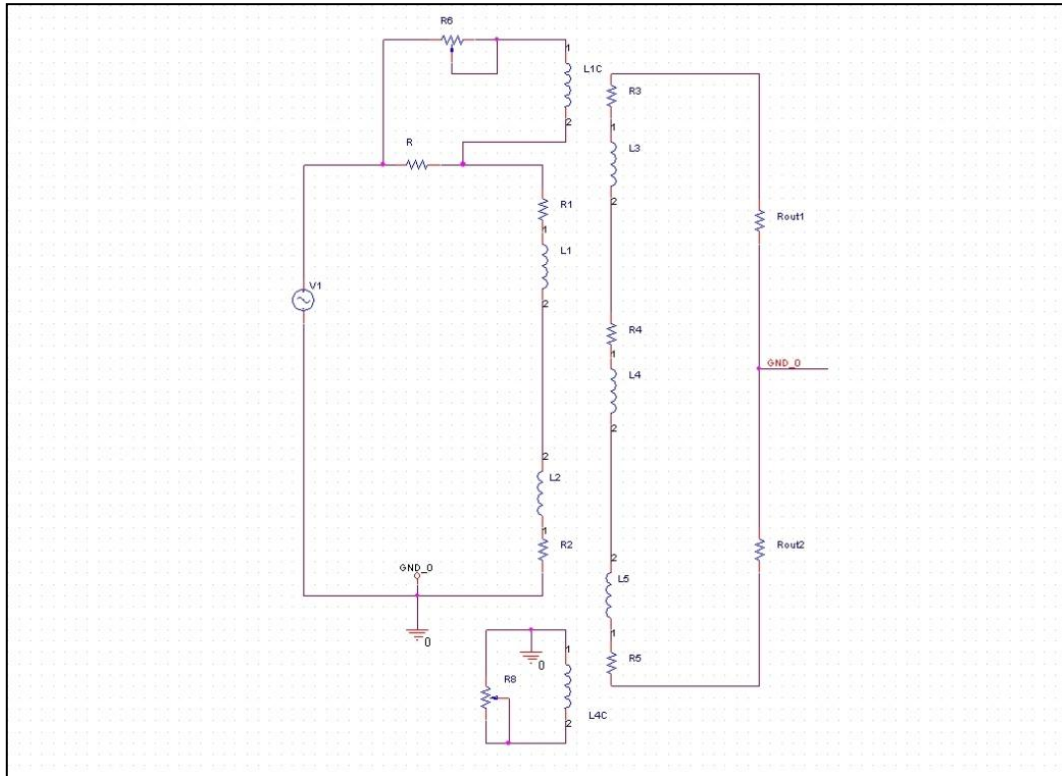


Figure 17: Active balance coil L1C and passive balance coil L4C(config. VII)

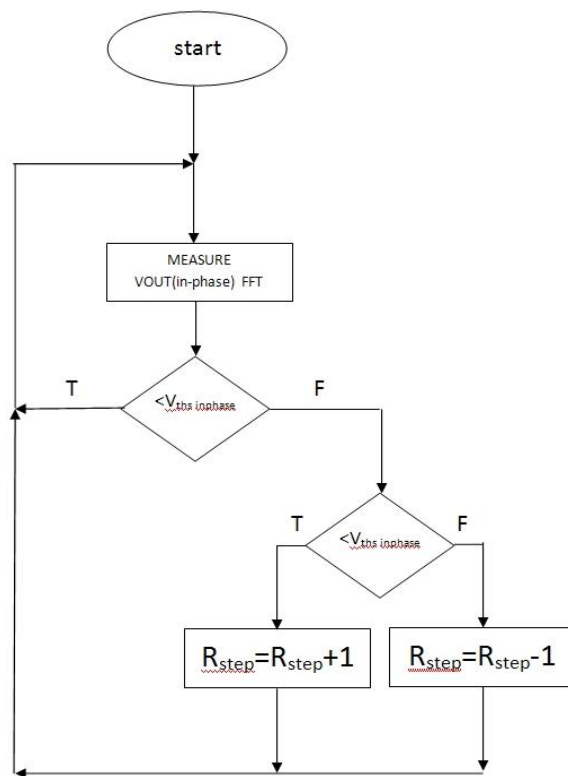


Figure 18: Flowchart of automatic balancing system

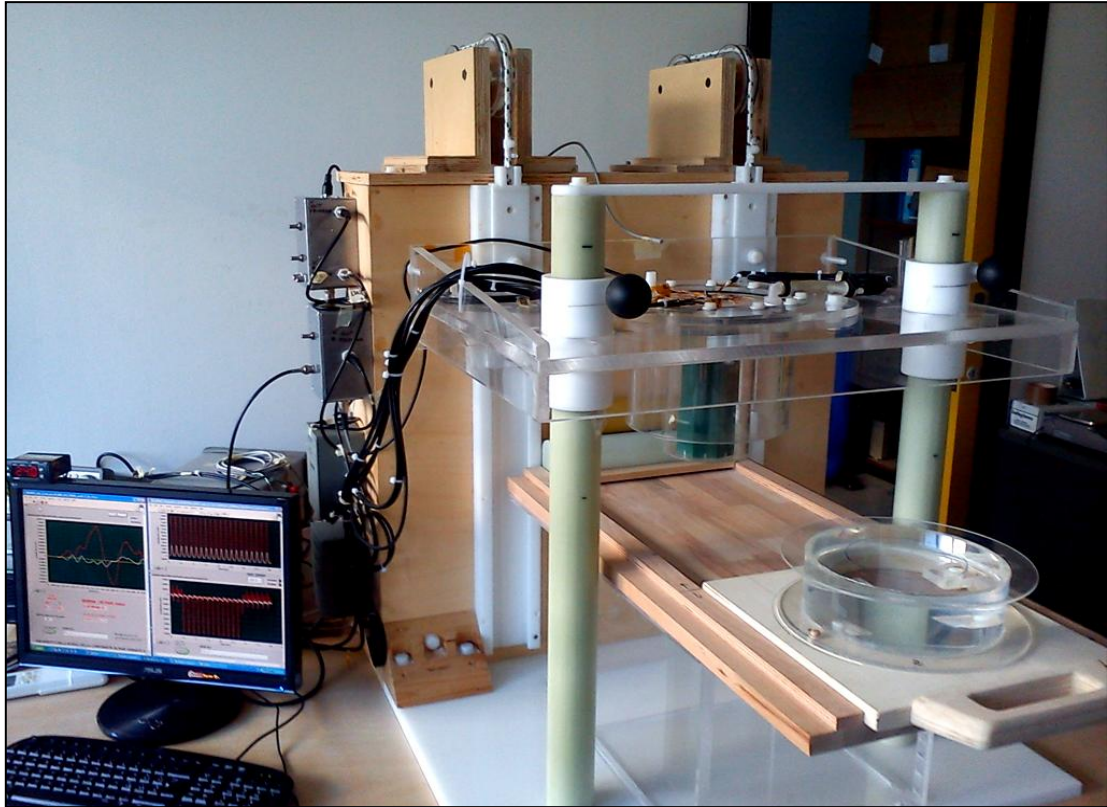


Figure 19: Susceptometer layout

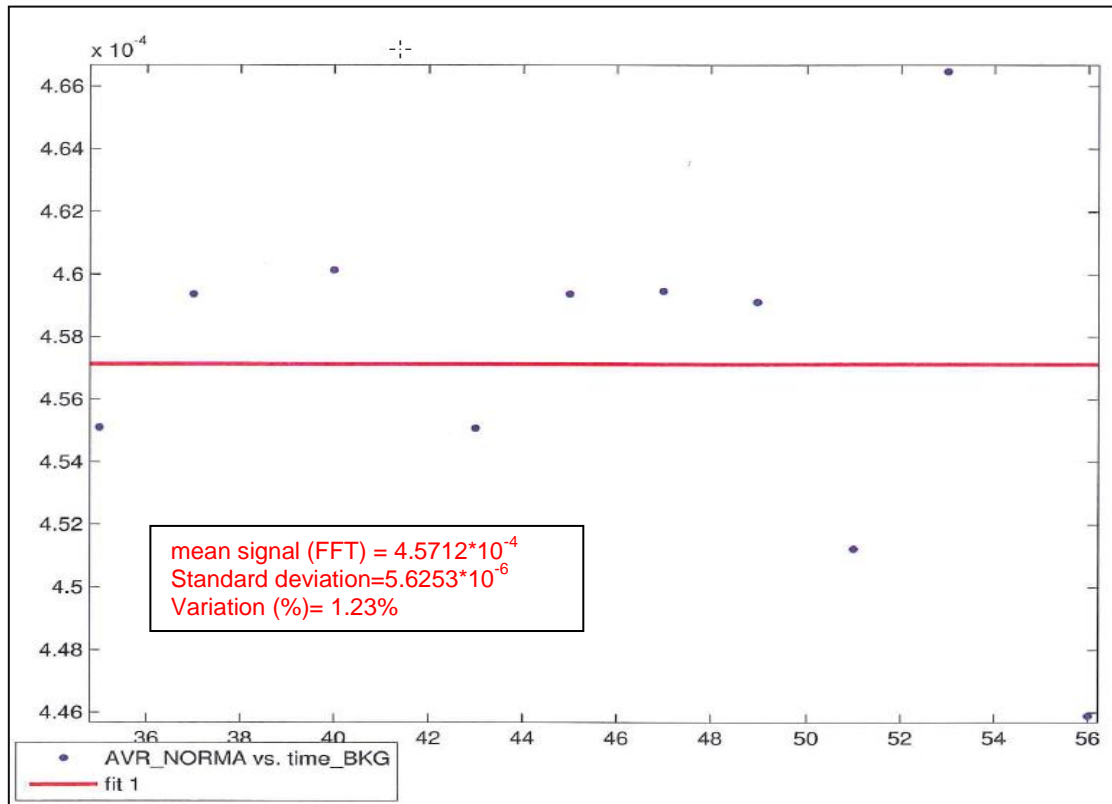


Figure 20: FFT signal changing during 30 minutes (T_{room} from 24.5°C to 24.6°C)

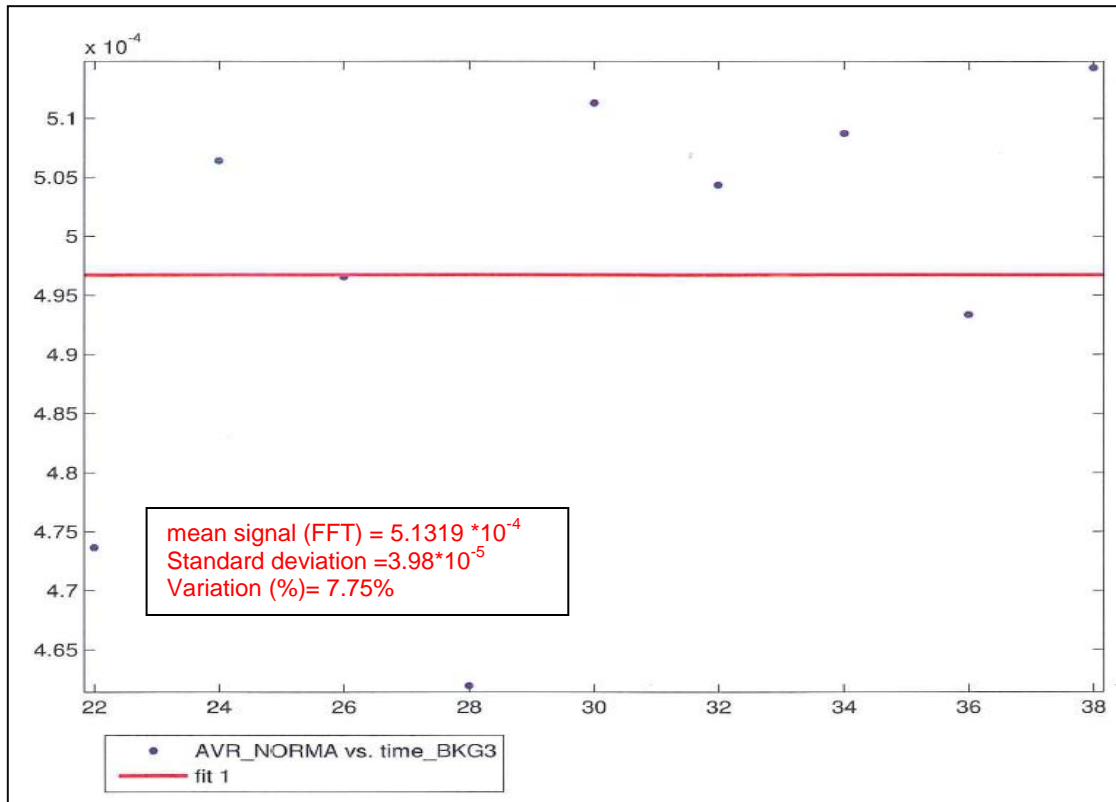


Figure 21: FFT signal changing during 30 minutes (T_{room} from 24.7°C to 24.8°C)

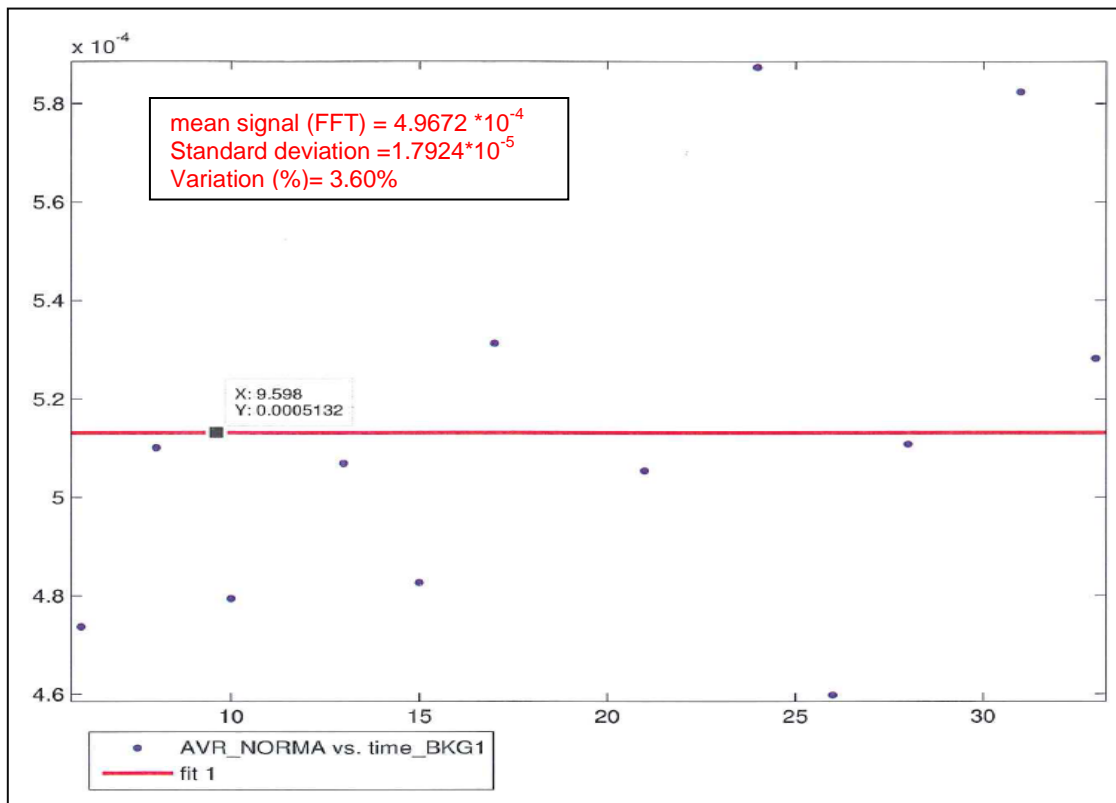


Figure 22: FFT signal changing during 30 minutes (T_{room} from 24.1°C to 24.5°C)

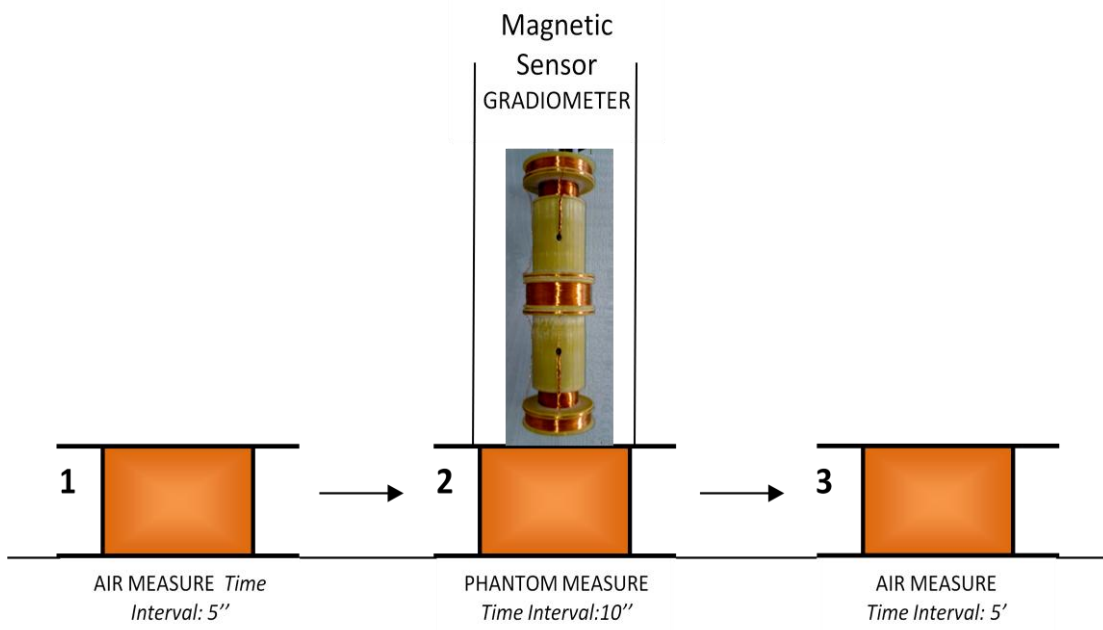


Figure 23: Acquisition timing (AIR – PHANTOM – AIR)

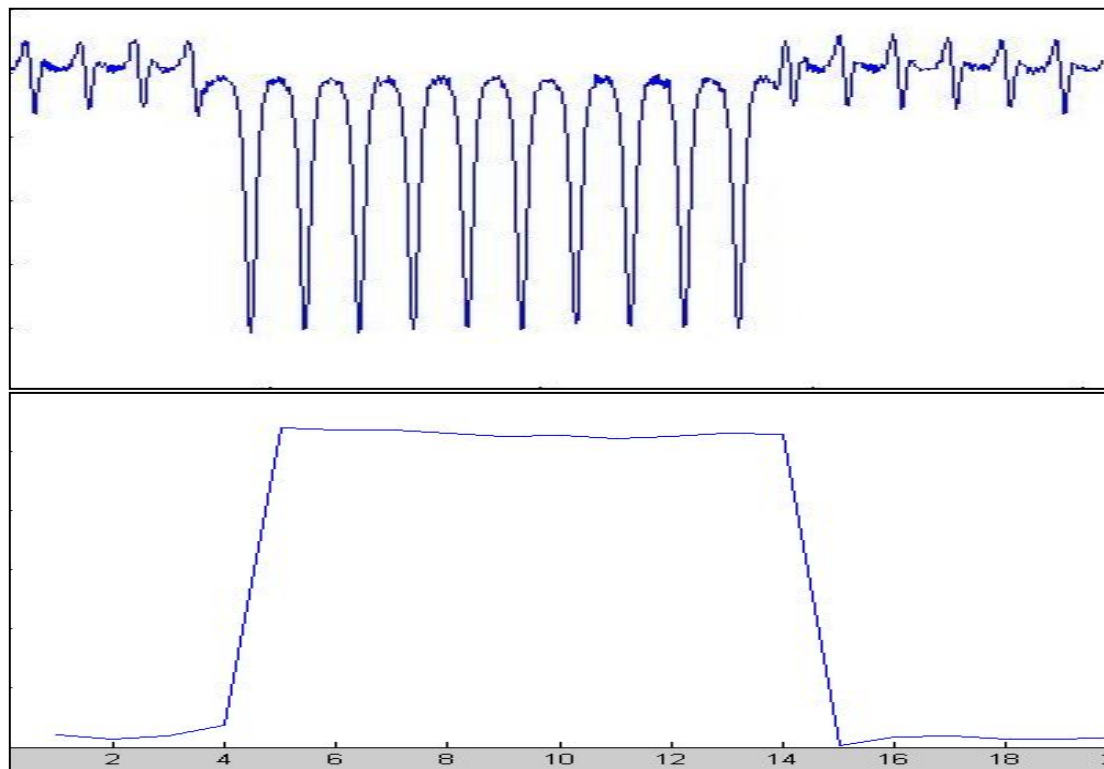


Figure 24: Output acquisition signal (in up the output signal vs time, in down the FFT output signal vs time)

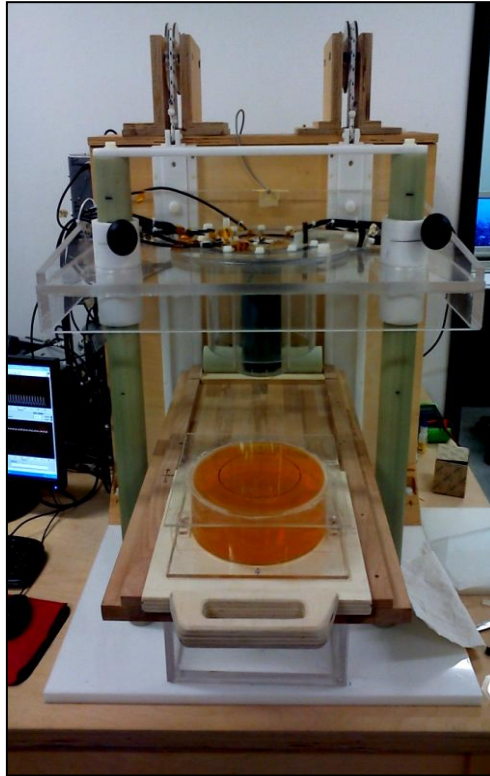


Figure 25: Phantom filled with Ferric Chloride

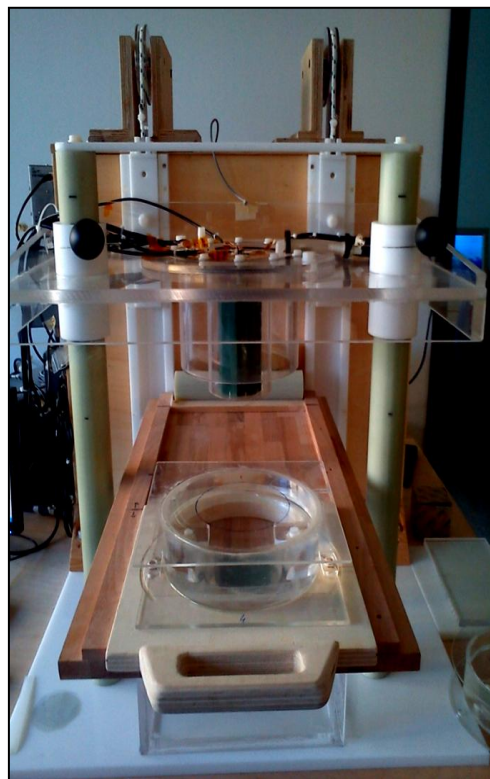


Figure 26: Phantom filled with water

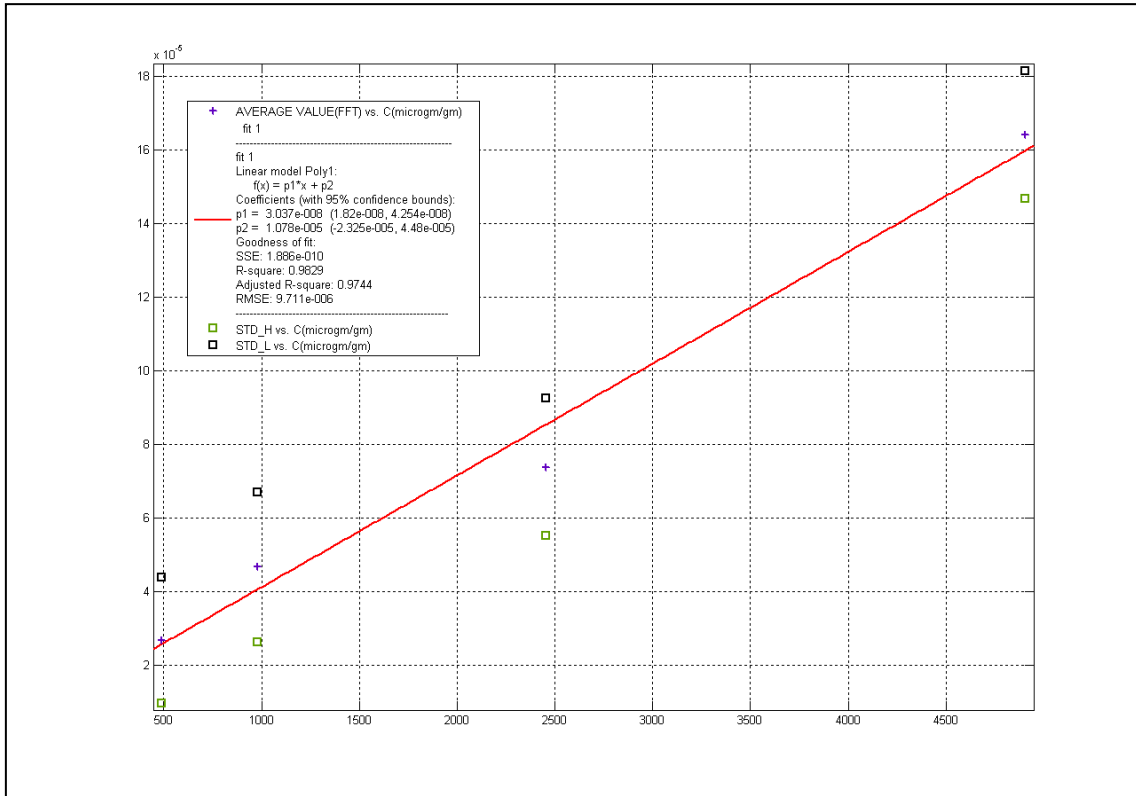


Figure 27: Calibration line: signal FFT(average value) versus concentrations



Figure 28: Latex Waterbag

Chapter 4 A Finite Element Analysis of 3D Anatomic Human Foot with plantar Fat Pad

4.1 Abstract

Background: In many application area there is an interest to understand the states of stress and strain in the tissues of the ankle-foot complex, together with the map of plantar pressures

Objective: In this work a preliminary prediction of stress condition of the foot with the real Plantar Fat Pad is presented: it was shown to play a very important role in the transmission of stress during the contact with the ground.

Design: The 3D foot model is the final result of 3D reconstruction applied in Computed Tomography scan DICOM standard images, FEM Modelling and Analysis.

Setting: Interaction Module of FEA has permitted to model cartilage only with the surface-surface contact. In this model the real morphology of Plantar Fat Pad has been considered. Plantar Fat Pad material has been modeled as elastic in agreement with the soft tissue model. The balanced standing condition was simulated. The contact pressure distribution on foot plantar area and stresses on the bone structures are calculated for a rigid contact between the plantar foot area and the rigid support.

Main Outcome Measures: To obtain the experimental data to compare the predictions of model, has been carried out a posturography static examination test, on a fixed baropodometric platform. Contact pressure values on the heel region and a metatarsal heads has compared and processed with FEA results

Results: The FEA predictions of plantar pressure distribution were in good agreement with experimental results, nominally, the peak value zones a the centre of heel region and beneath the metatarsal heads

Conclusions: The methods can be a very powerful to understand the foot and its implications in the project: a great variety of insole geometries and insole material could be tested with good approximation to study and improve the life style of patients with foot diseases and to design shoes for sport activities.

4.2 Introduction

In many application areas there is an interest to understand the states of stress and strain in the tissues of the ankle-foot complex, together with the map of plantar pressures. In clinical settings, such information would allow to assess the effect of anatomical variations and/or structural stress on the foot, providing medical support in the selection of clinical and surgical strategy to be adopted. In the footwear industry, the prediction of the stresses and deformations of the structures of the foot would be to support the design of the shoe, allowing you to assess whether or not the prototype satisfies the biomechanical objectives for which it was designed. In the sports sector, such prediction may help to understand the mechanisms that lead to stress fractures or overload pathologies in the foot. The quantification of the field of stress and strain is not determinable, until now, in vivo in the ankle-foot complex. Actually, there is no instrument capable to quantify non-invasively the mechanical stress of the foot. For this reason, numerical models have been developed, with a certain degree of approximation, to predict the distribution of stresses in the internal structures of the foot. These models, when rigorously validated, allow you to develop different studies, with a considerable saving in time and costs compared to traditional experimental studies on volunteers or cadavers.

Until now, it has been proposed in the literature numerous biomechanical models of the foot. The first formulations were trying to explain the anti-gravitary function of the foot, in which the structure was shaped like a simple architectural element such as a bow, an arch and a truss, or as the complex tripod and the more common backward helix (Figure 29).

More recently, due to the increased computational power of computers, the foot is represented by numerical models that can simulate load conditions and constraints more sophisticated and, at the same time, to find more accurate solutions in less time (Figure 30).

The models, developed with the 3D finite element technique, seem to achieve the best results in terms of reliability to the real kinematics and dynamics of the ankle-foot complex, compared to other types of models in the literature (1, 2, 3, 4, 5). These models utilize imaging techniques, such as computed tomography and magnetic resonance imaging to extract the right bone morphology for an human subject and use the ability of the finite element method (FEM) to solve

partial differential equations in domains complex and to obtain accurate solutions in a quick time.

In the literature, there are more studies(1, 2, 3, 4, 5) that have developed 3D finite element models of the foot in order to simulate the biomechanics. They, mainly, differ in the type of simplification measures in relation to structures geometry, materials definition, interaction methods between parties, definitions of loads and boundary conditions.

Concerning to the geometry of the model, generally only the bones are represented with their real morphology and, in some cases, also the cartilaginous-ligament structures. In contrast, the real morphology of the fat pad (or Plantar Fat Pad, PFP) under foot has never been considered in the literature models. In last works, the mechanical behavior of the PFP is modeled by assigning the mechanical properties of the generic volume, interposed between the skeleton and the plantar surface (1, 3, 7). In a previous study (2) it was shown that the heel fat pad (or Heel Pad HFP) has a complex morphology that can play an important role in the transmission of stress during the contact with the ground (Figure 31): the strains, transmitted from the ground to the foot during a step, will not reach high values, but the repetitive motion can lead to excessive stress of the leg. The most critical stage is the first foot-ground contact (or heel strike): in this phase, the first damping mechanism is the PFP, natural pressure reducer of the foot by Heel Fat Pad (HFP) and by the metatarsal fat pad (MFP), respectively, located under the heel and under the metatarsal heads. PFP has a structure composed of fat lobules contained in a dense network of fibro-elastic septa, which makes its capable to absorb the energy produced in the impact foot-ground, to redistribute pressure on larger surfaces and, simultaneously, to provide the elastic come back to start new step.

In this paper, the objective is the creation of ankle-foot complex for subject-specific model including the morphology dell' PFP. This model will be developed using the finite element method from 3D computed tomography data. The model will be validated by comparing the results of finite element simulation in static loading conditions with those obtained experimentally by baropodometric examination. Despite the geometric complexity of HFP, the FEM models of 3D foot shape, the adipose tissue is modeled assigning the properties of the material deriving from experimental trials(6).

4.3 Methods

4.3.1 Geometry Modelling

The methodological approach used to model the 3D geometry of the foot and its structures characteristic was obtained in three successive stages.

Computed tomography scan

We have studied with computed tomography scan right foot and ankle of a volunteer male of 26 years (weight 80 kg , height 186 cm), which he has never reported significant podalic trauma.

The subject to be tested was chosen from a large series of healthy subjects. It has used a Philips Brilliance-64 CT scanner (Philips Medical Systems, Cleveland, Ohio) to acquire 70 slices with a thickness of 0.8 mm , with an overlap of 0.4 mm between adjacent slices (Figure 31, left) . The acquisition protocol is the one described by Campanelli et al. in which it is sought to maximize the neutrality of the joint angles of the ankle and foot (2)(Figure 31, right). The CT data were filtered with a filter both for the soft tissues (to facilitate the segmentation of the fat pad), and for hard tissue (the bones segmentation of the foot). Two different sets of images were obtained and converted to DICOM format (Digital Imaging and Communication Format).

Segmentation

The DICOM data were imported into Amira 3.1.1 (Mercury Computer Systems, Chelmsford, MA, USA) to reconstruct 3-dimensional models of foot, ankle, bones and fat pad. The segmentation of the bones has been obtained by semi-automatic tools (mainly by the *blow tool*, based on a semi-automatic method) and done manually slice to slice. In all, 30 foot bones and the distal parts of the tibia and fibula were segmented. In contrast, the Plantar Fat Pad has been segmented in manual mode, since it is constituted by two parts with different density(fat and connective septa). The contours obtained from each slice were interpolated to obtain polygonal surfaces for the HFP and bones. The 3D data obtained were exported as stl format (Stereolithography), by defining a 3D surface with the union of triangular surfaces oriented or meshed. These surfaces generated are often full of imperfections such as holes: to eliminate these problems we made use of the software MeshLab, which through the tool Cleaning and Repairing allows you to fill and eliminate such defects. This geometry is now being exported to PLY format (Polygon File Format).

Mesh Generation and Correction

The surface mesh for each bone geometry, encoded in PLY format, is reconstructed and turned in Solidworks CAD (SolidWorks Corporation, Massachusetts, USA) by the tool "Mesh Prepaing Wizard". The mesh will have created with the IGES format, compatible with ABAQUS, and finally by the tool ABAQUS (Geometry Repair) will be able to eliminate imperfections and self-intersecting geometries. Below is a diagram of the methodology adopted for 3D modeling (Figure 33).

4.3.2 Finite element Modeling

The 3D finite element model was imported and assembled in to the full non-linear FEA package ABAQUS 6.10.1 (ABAQUS, Inc., Dessault Systemes Simulia Corp., Providence, RI, USA). It

is shown in Figure 34 and consists of 30 bones, and includes all the distal phalanges, 3 proximal and medial cuneiform, talus, calcaneus, cuboids, navicular, tibia and fibula, and 2 sesamoids: inside the software the interactions between the parts, domains of equations, boundary conditions and solution methods were defined.

Objective of this study is to extract information on the stress and strains within the structure of the foot and on the pressure exerted of the plantar fatpad, during the application of a static load. It is assumed that the foot touches a slim ideal and rigid: a model of an "earth" plan is added to model.

4.3.3 Interactions between parts

ABAQUS does not recognize any kind of mechanical contact between the parts of the model IF they are not specified in the " interaction form": two close surfaces need to have specified an interaction between them.

BONE-BONE INTERACTION (CARTILAGE)

The 30 bones of the foot-ankle complex interact through 41 facet joints (4 for ankle and 37 for foot, including two sesamoids). To simulate the surface interactions between the bone structures, ABAQUS uses an automated algorithm to model surface contact. Due to the lubricated nature of the articular surfaces, the behavior of the tangential contact between the articular surfaces was considered without friction, whereas the normal state is considered to be linear with contact stiffness equal to 10 MPa. The cartilage definition has been deduced through the virtual anatomical models of Primal Pictures (Interactive Foot and Ankle, Primal Picture Ltd., UK) and the manual of Gray (Figure 33, right) . It should be noted that previous studies (3) modeled cartilage with a 3D polygon mesh, obtained from the Boolean subtraction between the bone and interposed volume. This mesh was glued to the articular surfaces by mesh tie constraints. Our studies and tests on the subject have shown that it was possible to create such modeling in ABAQUS simply through an interaction sup-sup, an automatic algorithm capable to simulate the contact of surfaces and to remove any overclosure problems: this assumption allowed less energy and less computational cost.

BONE - FATPAD INTERACTION

The contacts between the calcaneus and fat pad and between the metatarsal heads and the fatpad have been defined through tie constraints: an automated algorithm of ABAQUS maintain in contact two regions (Figure 36). The virtual combination between the two structures was chosen to simulate their real anatomical union: the calcaneal fat pad is physically attached to the posterior-inferior portion of calcaneus through a dense network of connective septa: two surface has been modelled without relative and rotational motion. Therefore, the surfaces of the calcaneus and the metatarsal heads were defined as master surface, however, the surfaces of the Fatpad as

slaves. The real nature of the anatomical region suggests to join fatpad together all metatarsal heads except for the first, which is attached via 2 sesamoid bones(Figure 36).

FATPAD - GROUND INTERACTION

A flat rigid horizontal has been used to model the support of the foot on the ground. The interface foot / floor has been defined by a contact surface, which allows the transmission of the load from the hard floor to the foot. The type of approach used to simulate this interaction is of the small- sliding tracking node -to-surface contact with tangential and normal. The surface of the fatpad was defined as the slave surface and the rigid support of the plan as a master surface. The normal contact was defined using the Augmented Lagrange method constrains, already automated algorithm in ABAQUS . The tangential contact between soil and fatpad was set to 0.6 using the model of Coulomb friction (8-12)(Figure 37).

4.3.4 Property of Materials

All materials were considered isotropic and linearly elastic. The bone behavior was assigned linearly elastic with Young's modulus and Poisson's ratio, respectively, equal to 7300 MPa and 0.3. These values were estimated by averaging between cortical and trabecular bone, by weighing the contribution in amount of the volume, according to the model of Nakamura et al.(9)

4.3.5 Load and Boundary conditions

For this study, the load was considered static (Figure 32): the ground is in the bottom and the strength is applied on the tibia and the fibula, leaving the foot in a natural way to move toward the floor. This method is suggested by Ref (7, 13). Until the 1970s it was thought that the whole load on the body weight to be transferred to the foot only through the tibia-thallus joint, the it is thought fibula to have only the stabilizing function of the ankle. In 1971 Lambert measured the load capacity of the fibula by "strain-gauge" (SG), establishing that the fibula carries one-sixth (17%) of the applied load. Later, in 1984, *Tabeke* claimed that 17% of the load was an overestimate and by force transducers [27], placed within portions of two severed bone, he estimated that the fibula was carrying only 6.4% of the total load(7). In Table 10 it shown the load values found in the literature for the fibula. Based on these considerations (13), we divided the 10% of half of the body weight of the subject (450 N) on the fibula and the remaining 90% on the tibia. In particular, the upper tibia and fibula surfaces are equal at 5.58 cm² and 1.74 cm². In this configuration, the ground was considered linearly elastic with Young's modulus and Poisson's ratio, respectively, equal to 17000 MPa and 0.1.

The applied force has an amplitude as smoothing step (Figure 38).

4.3.6 Mesh Generation

A large variety of solid elements in ABAQUS package can be used for modeling the foot and the ankle. Among all continuous elements, hexahedral elements usually give higher accuracy in the solution by a lower computational cost particularly considering complex structures with large deformations. However, due to the limitations of the algorithm automated meshing in hexahedral mesh ABAQUS to build structures of irregular shape, to mesh foot bones and soft tissues, such as the fatpad, the tetrahedral elements with 4 nodal elements was used. Because of incompressible nature and regular geometry of the rigid ground, it was meshed with hexahedral elements. In Figure 39, it shown a full view of the mesh of the 3D foot model.

4.4 Results

To verify that these assumptions do not affect the prediction of the model, you need to do a validation. To obtain the experimental data to compare the predictions of the model, has been carried out a posturography static examination test, on a fixed baropodometric platform (WINPOD - IMAGO CNS). Contact pressure values at the heel region and a metatarsal heads has been compared and processed using MATLAB(The Mathworks Inc., Boston, MA, USA) with FEA results(). Numerical simulations were accomplished in about 300 min on a PC DELL STUDIO XPS 435MT(Intel® Core i7 CPU 920@2.67GHz, RAM 10.0GB, WinVista 64bit).

The FEA model predicts maximum plantar contact pressure beneath 4th metatarsal of 94KPa and on the heel of 74KPa, the experimental value is 107KPa beneath 4th metatarsal and on the heel is 88KPa for pure compression and balancing standing case. By coregistration of image between experimental data and FEA predicted result the contact area approximately equal to 90cm², compared to 115cm² obtained from experimental measurement.

4.5 Discussions

In this study, a 3D anatomically realistic FE model of foot was established based on CT scan slices. In this model the main simplifications are as follows: (i) the ligaments weren't considered: several studies show that under conditions of upright posture and static load, the balance is maintained only with the single congruence of the articular surfaces, (ii) the geometry of the cartilage has not been modeled, which are modeled as an interaction surface-surface,(iii) assumption of non linear hyper-elastic material law for the fatpad, (iv) simplified bone structures (no cortical and trabecular regions).

The experimental plantar contact pressure distributions is qualitatively comparable with the predicted FEA results, nominally, the peak pressure values zones at the centre of heel region and beneath the metatarsal heads. However in the quantitative point of view the FEA results are

higher than experimental results. The difference may be caused by the resolution of pressure that report an average pressure over a sensor area while the FEA model reports the contact pressure as calculated from a node force per element's surface area.

The stress distribution pattern was similar to those experimental data in literature (4, 16, 17), in which the relatively higher stresses were located in the rearfoot and forefoot. It also can be found from Figure 40 that the position and peak value of the stress concentration were comparable with those published experimentally measured plantar pressures (4, 16, 17).

The difficulty in obtaining a completely static posture that replicate the FEA model load conditions was a major experimental problem encountered and an aspect that must be accounted during the results and discussions.

4.6 Conclusions

FEA(Finite Element Analysis) Models can be a very powerful method to understand the foot mechanical behaviour and its implications to human comfort. For the purpose, an anatomically detailed foot model was generated from CT scan image data, using segmentation and reconstruction techniques and 3D CAD modelling. The monitoring of plantar pressure at the foot plantar with the fat pad Plantar model will be the main objective. Achille tendon and plantar fascia weren't introduce. For this purpose, the effect of the magnitude of load at the Achille tendon will be studied in order to understand the effect on the contact pressure distribution, contact area and coordinates at the center of pressure.

After the conclusion of the experimental tuning procedure, a wide variety of insole geometries and insole material can be tested to study and improve the life style of patients with foot diseases, such as pronation, painful syndrome, arthritis syndromes, etc.

4.7 References

1. Antunes, PJ, Dias, G.R., Coelho, A.T., Rebelo, F., Pererira, T.: Non-Linear Finite Element Modelling of Anatomically Detailed 3D Foot Model Available online.
2. Campanelli, V; Fantini, M; Faccioli, N, et al.: Three-dimensional morphology of heel fat pad: an in vivo computed tomography study. *J Anat.* 219: 622-631. 10.1111/j.1469-7580.2011.01420.x
3. Cheung, JT; Zhang, M; Leung, AK; Fan, YB: Three-dimensional finite element analysis of the foot during standing--a material sensitivity study. *J Biomech.* 38: 1045-1054. S0021929004002842 [pii]10.1016/j.jbiomech.2004.05.035
4. Cheung, JTMaZ, M.: Finite Element Modelling of the Human Foot and Footwear. 2006 ABAQUS Users' Conference.
5. Franciosa, P, Gerbino, S.: From CT Scan to Plantar Pressure Map Distribution of a 3D Anatomic Human Foot. Proceedings of the COMSOL Conference 2010 Paris.
6. Lemmon, D; Shiang, TY; Hashmi, A; Ulbrecht, JS; Cavanagh, PR: The effect of insoles in therapeutic footwear--a finite element approach. *J Biomech.* 30: 615-620. S0021929097000067 [pii]
7. Raumer, A: Valutazione della Biomeccanica e della cinematica dell'articolazione della caviglia con particolare riguardo ai legamenti. Padova, Università degli Studi di Padova, Facoltà di Ingegneria
8. Zhang, M., Mak, A.F.T. In vivo frictional properties. *Prosthetics and Orthotics International*, 1999
9. Nakamura S., Crowninshield R.D., Cooper R.R.,; An analysis of soft Tissue Loading in The Foot: a preliminary Report; *Bulletin of Prosthetic Research*; 1981
10. Cheng J. T., Zang M., Kai-Nan An; Effect of plantar fascia stiffness on the biomechanical responses of the ankle-foot complex; *Clinical Biomechanics* 19; 2004
11. Lijun Wu; Non linear finite element analysis for musculoskeletal biomechanics of media and lateral plantar longitudinal arch of Virtual Chinese Human after plantar ligamentous structure failures; *Clinical Biomechanics* 19; 2004
12. M. Zhang, A. F. T. MaK; In vivo friction properties of human skin; *Prosthetic and Orthotics International* 1999, 23, 135-141
13. W.R Ledoux, E. DW Dengler. M J. Fassbind; A finite element foot model for simulating muscle imbalances, *Journal of Foot and Ankle* 2008, I (Suppl I):OD45
14. W.M Chen, Taeyong Lee, Peter Vee-Sin Lee, Jin WOO Lee, sung- Jae Lee; Effect of internal stress concentrations of plantar fascia soft tissue- a preliminary Three-dimensional finite element analysis; *Medical Engineering & Physics* 32(2010) 324-331.

15. Jacob, S., Patil, M.K., 1999 Three-dimensional foot modeling and analysis of stress of normal and early stage Hansen,s disease with musckle paralysis.J. Rehab. Res. Dev. 36, 252-263
16. Chen WP, Tang FT, Ju CW. Stress distribution of the foot during mid-stance to push-off in barefoot gait: a 3D finite element analysis. Clin Biomech (Bristol, Avon) 2001;16:614–20.
17. Tao K, Wang D, Wang C, Wang X, Liu A, Nester CJ, et al. An in vivo experimental validation of a computational model of human foot. J Bionic Eng 2009;6:389–97.

4.8 Tables

MATERIALS	YOUNG'S MODULUS	POISSON COEFFICIENTS	References
BONE	7300 MPa	0.30	Nakamura et al
FATPAD	1 MPa	0.45	Jacob e Patil 1999
GROUND	17000 MPa	0.1	T.-X. Qiu et al(2011)

Table 9: Properties of Materials

Proprietà	Lambert	Wnag	Takebe	Goh
Carico applicato (Kg)	68	60	60	235
Metodo	SG	SG	FT	FT
Posizione neutra	17%	11%	6.40%	7.12%

Table 10: Weight-bearing capacity of the fibula as a percentage of the total load. SG = strain gauge, FT force trasductors [7]

4.9 Figure

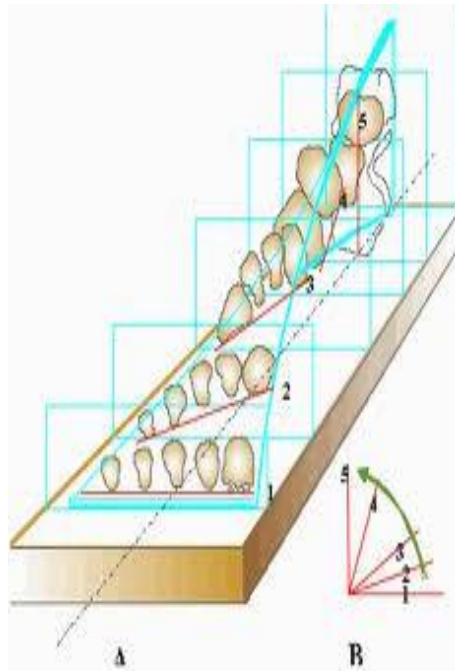


Figure 29: Backward helix

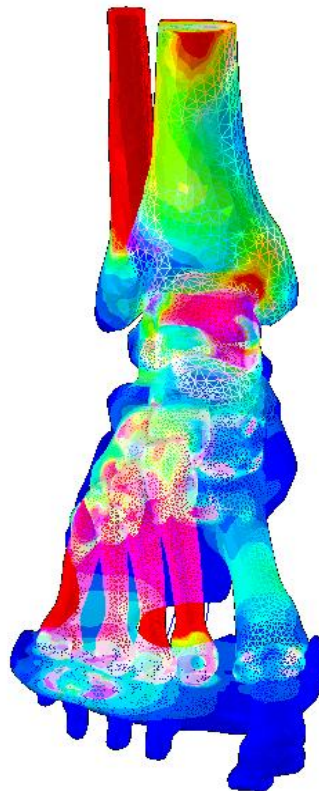


Figure 30: Finite element Model of the Foot

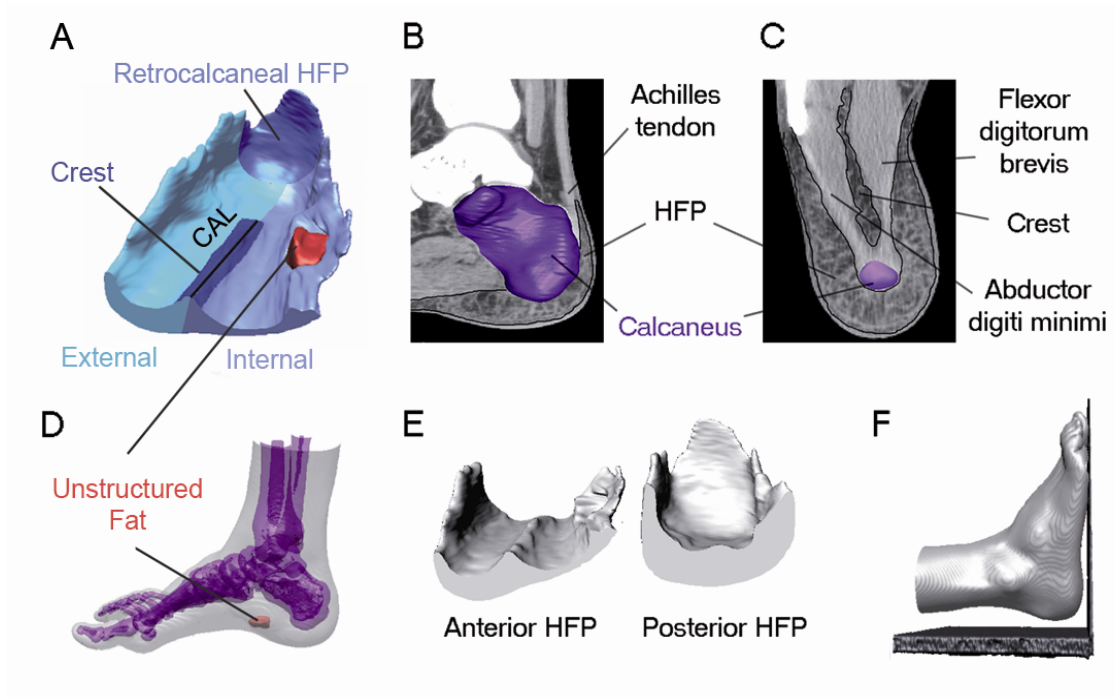


Figure 31: A) Morphology of HFP B) sagittal section of HFP in spatial relationship with the heel and the Achilles tendon, C) axial section of HFP in connection with the plantar muscles, D) non-structured portion of HFP; E) front and rear sections

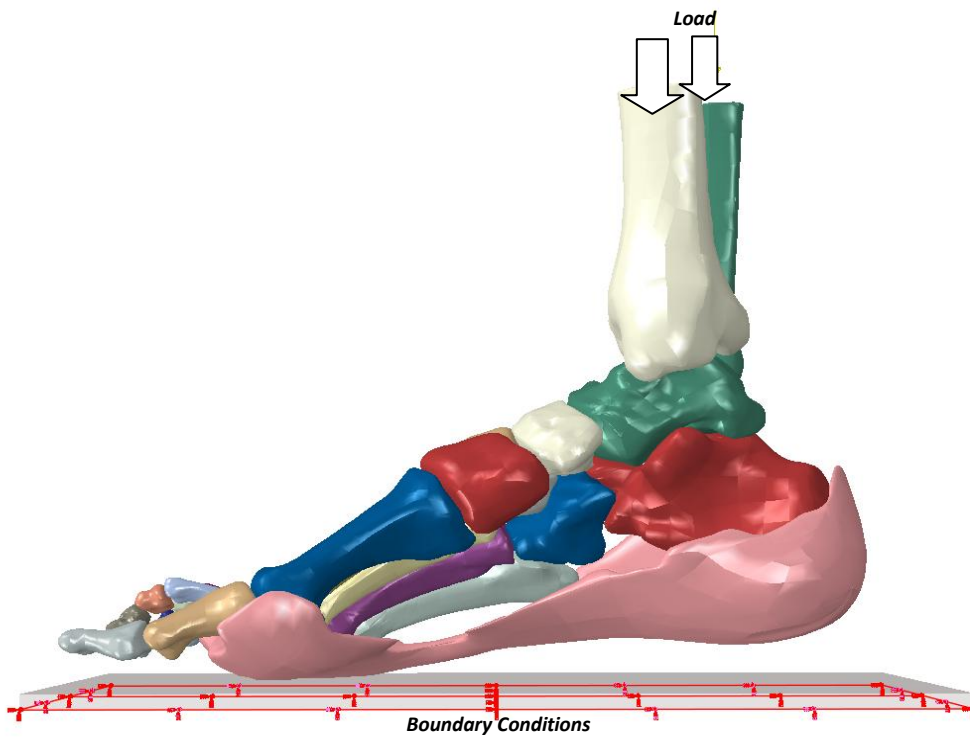


Figure 32: Loads and Boundary conditions

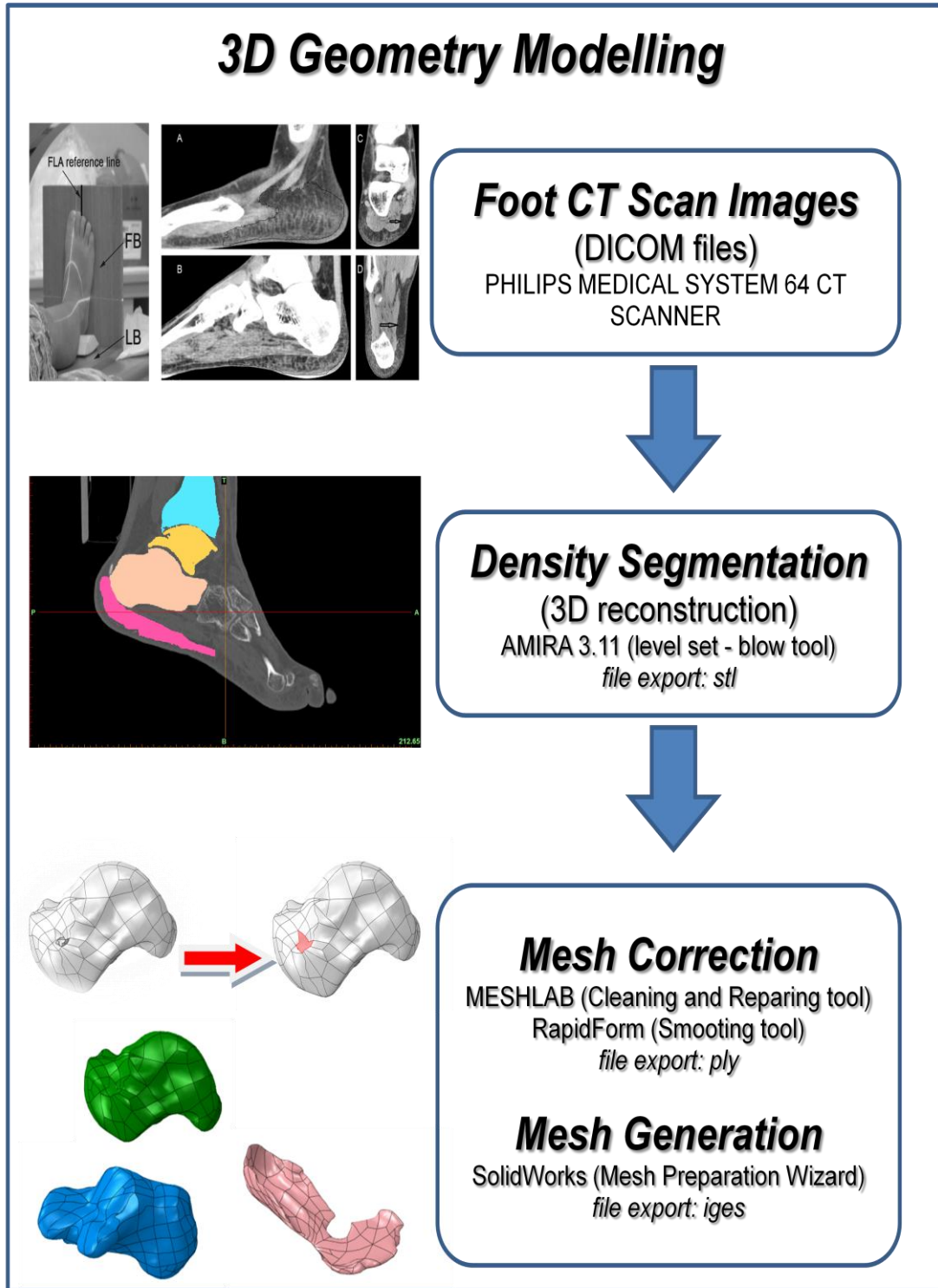


Figure 33: Workflow methodology for 3D Cad Modelling

In upper position, on the left: CT image acquisition of HFP, on the right: segmentation of HFP; In down Correction of the defects of the talus mesh made with the Repair Geometry tool in ABAQUS

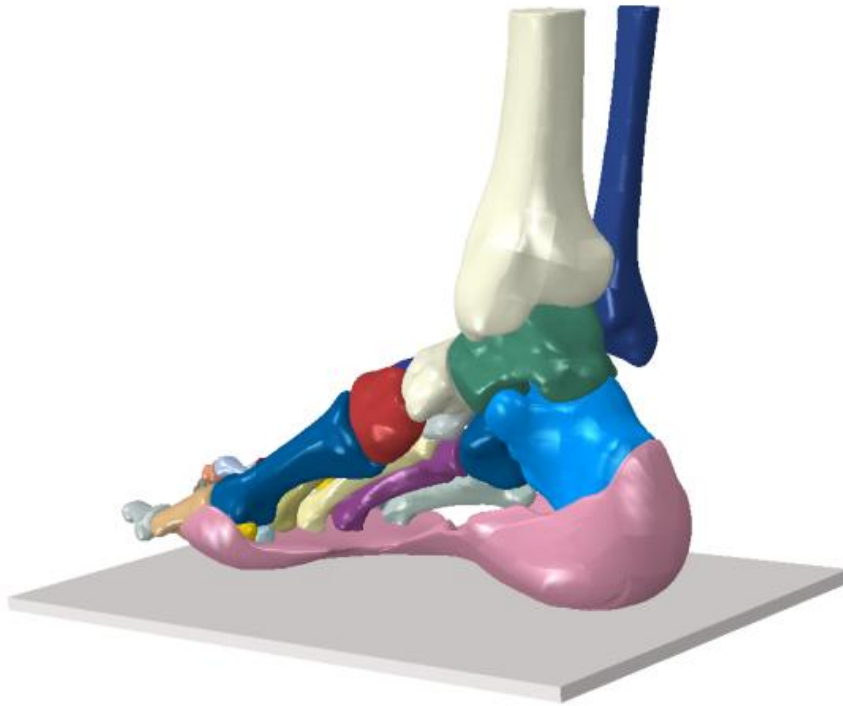


Figure 34: 3D model of the foot with together all the bones and plantar FatPad

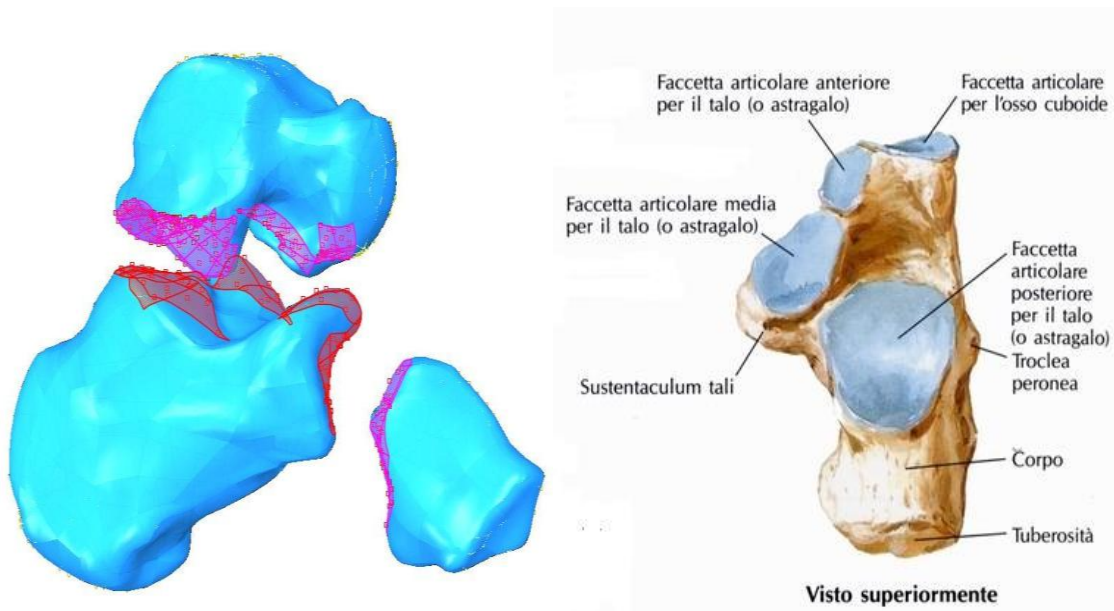


Figure 35: Left: Facet Joints of the calcaneus (and talus that articulates with the cuboid), right: the talus (by Drake, Vogl, Mitchell, Tibbitts and Rivhardson 2008)

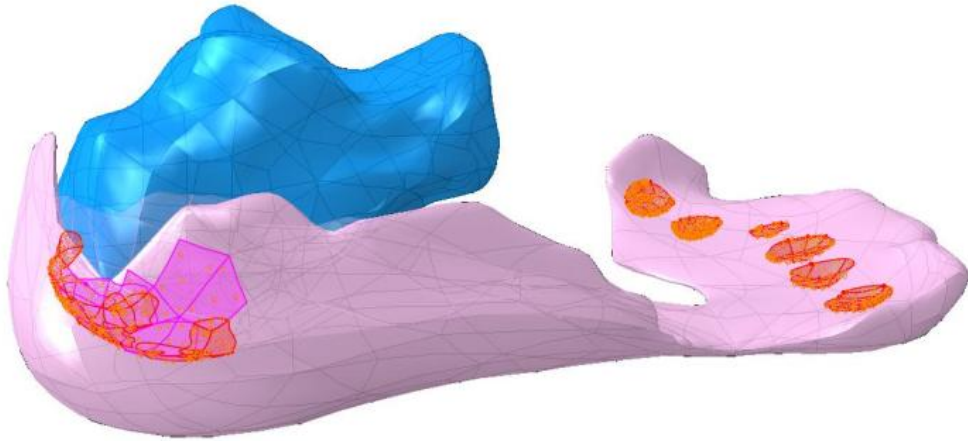


Figure 36: Interaction between the posterior inferior portion of the heel bone and fat pad (tie constrain interactions)

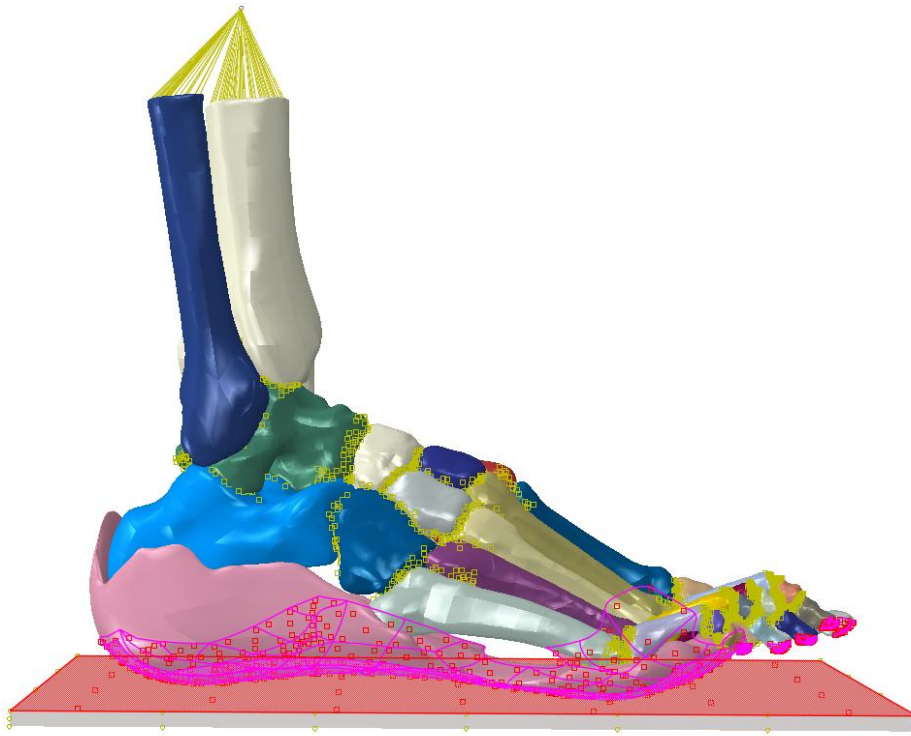


Figure 37: Interaction between the fat pad and the horizontal support

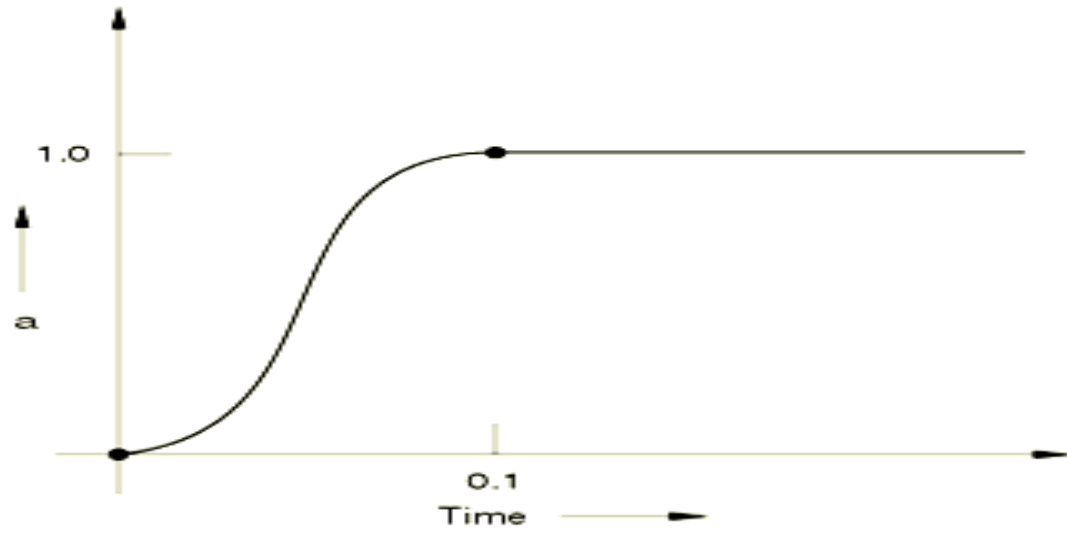


Figure 38: Smoothing step

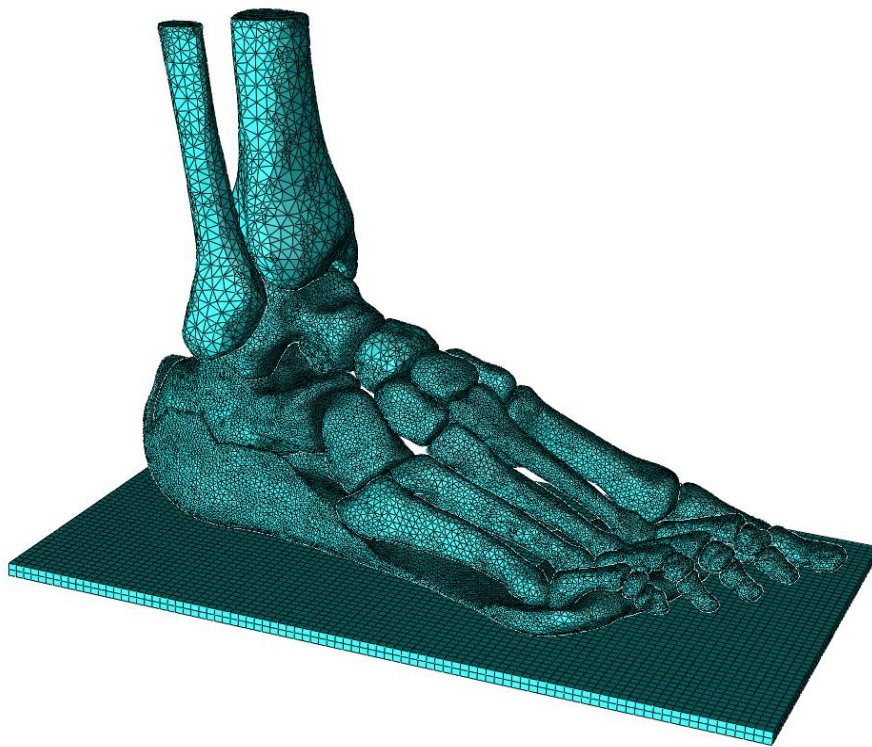


Figure 39: Global Mesh of 3D foot Model

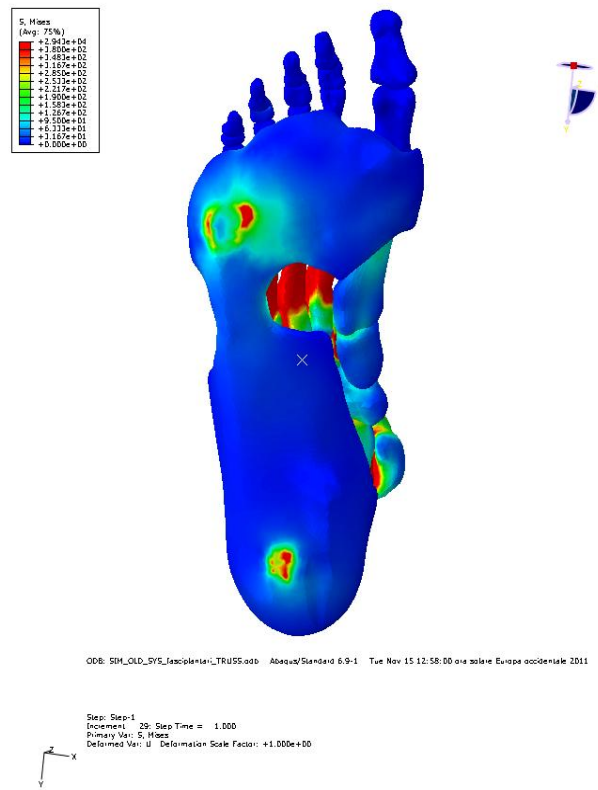


Figure 40: FEA Predicted plantar pressure on the plantar fat pad

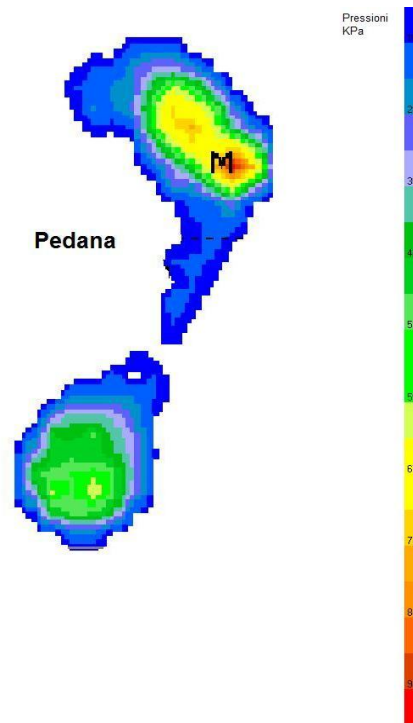


Figure 41: Experimental foot plantar contact pressure distribution on the baropodometric platform

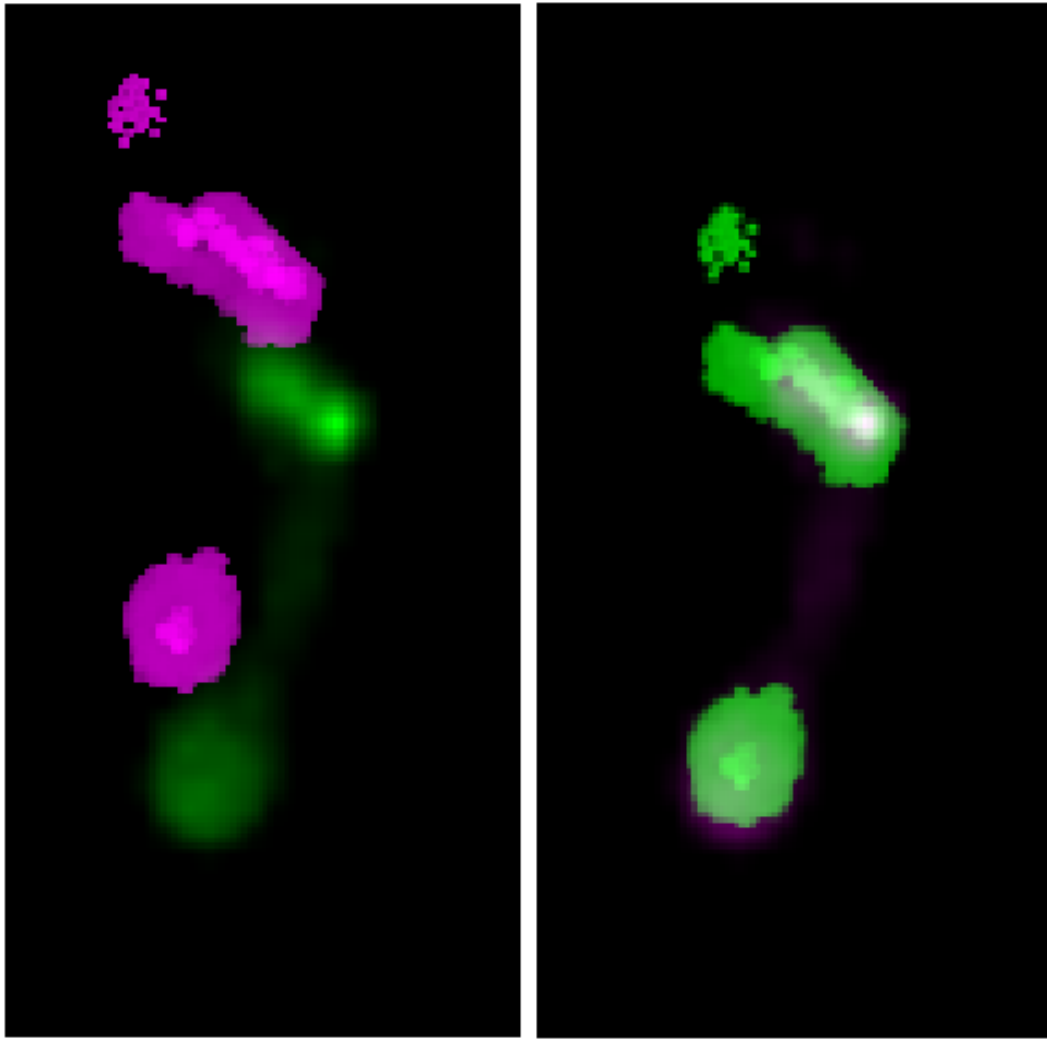


Figure 42: Co-registration of FEA predicted contact pressure on the ground (in violet) into experimental contact pressure on the baropodometric platform (in green).

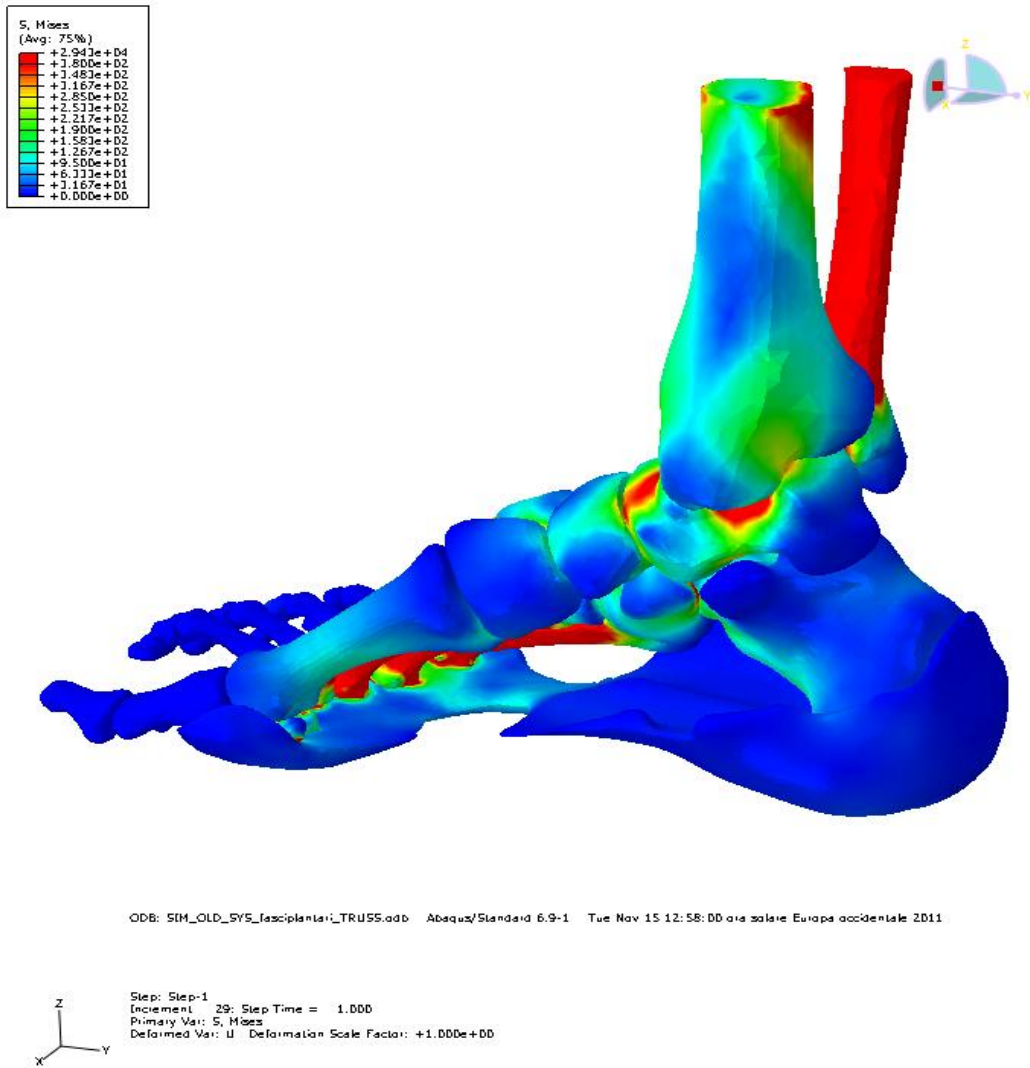


Figure 43: Von Mises stress(pure compression)

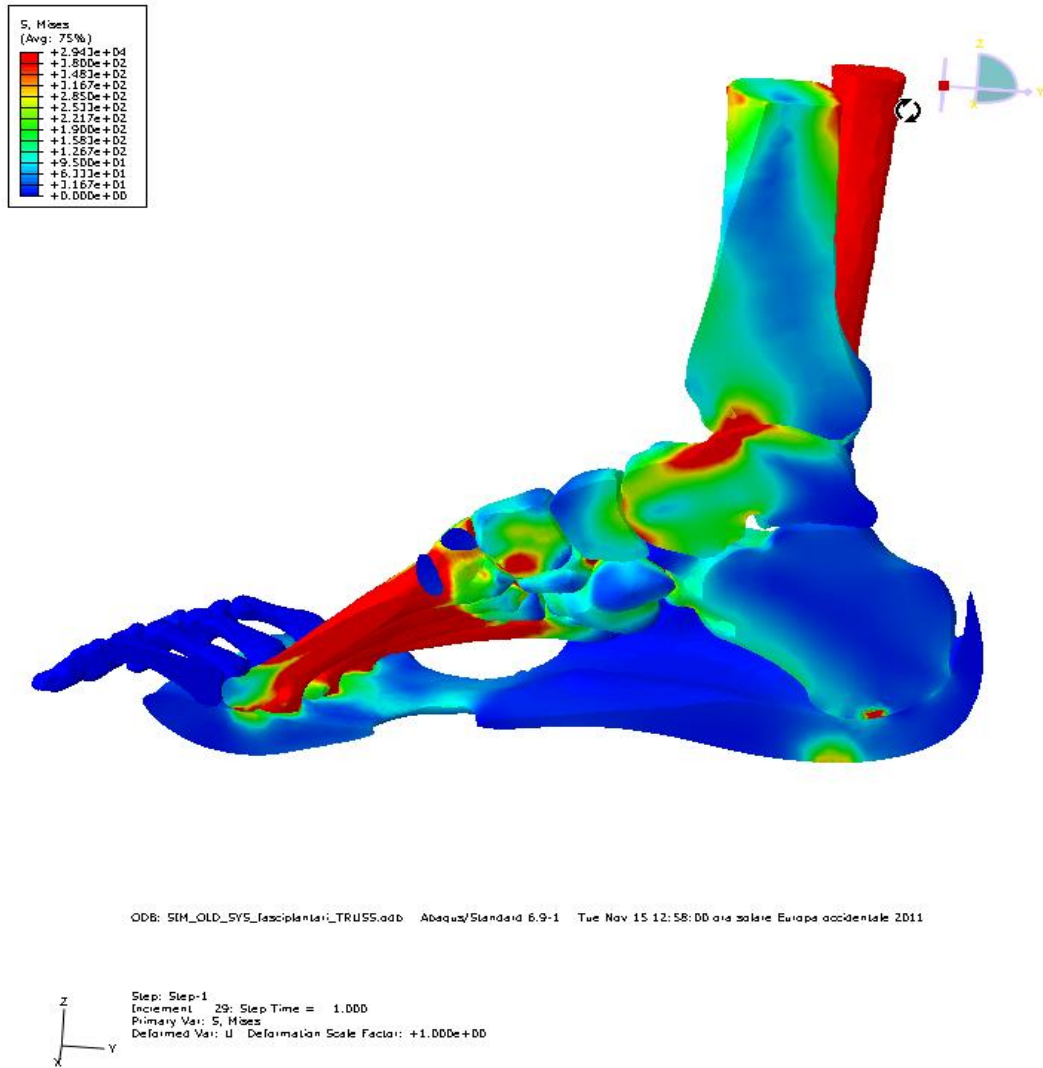


Figure 44:Foot section-cut (pure compression)

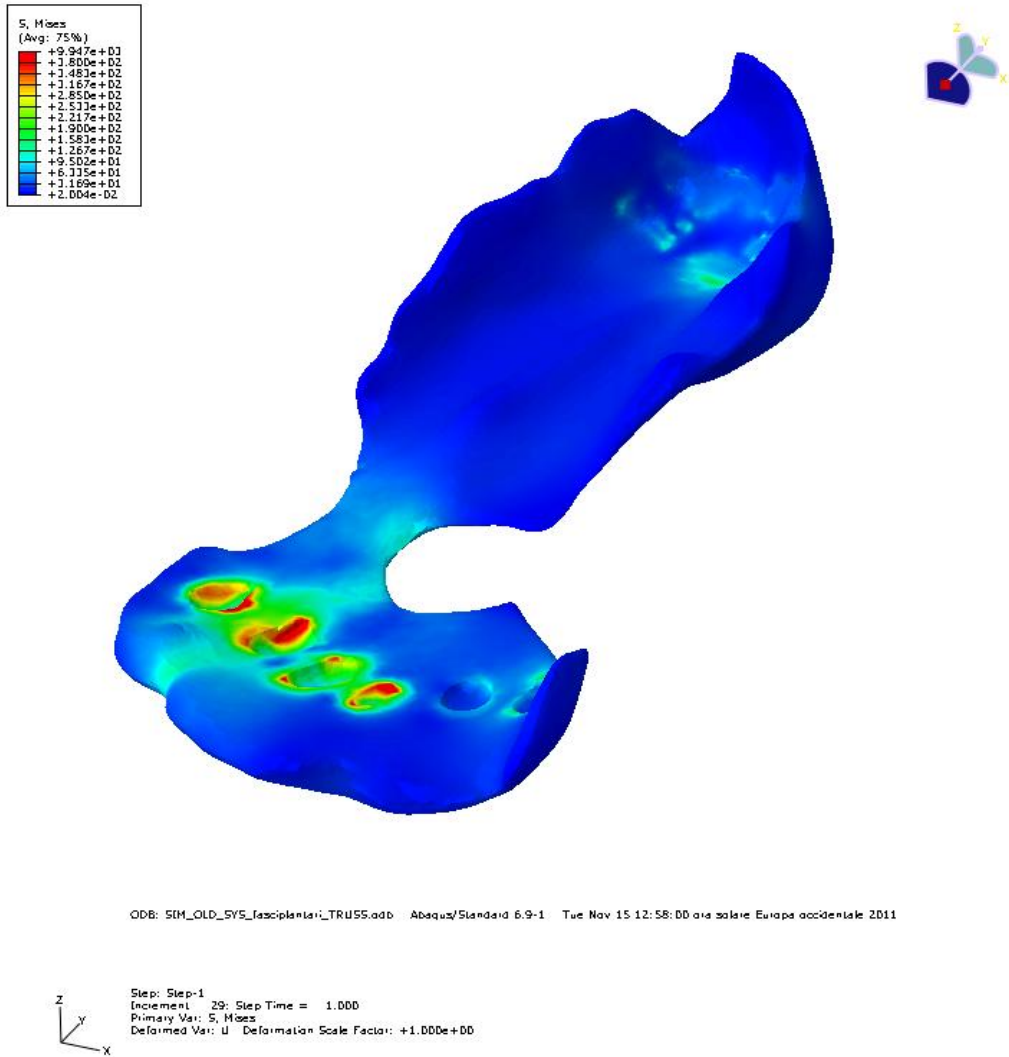


Figure 45: Von Mises Stress (pure compression) of plantar fat pad